University of Tokyo
Graduate School of Science
Department of Physics

Diversities out of the observed proto-planetary disks: migration due to planet-disk interaction and architecture of multi-planetary systems (観測された原始惑星系円盤からの多様性：惑星—円盤相互作用による移動と多重惑星系の構造)

Shijie Wang

A thesis submitted to
the graduate school of science,
the University of Tokyo
in partial fulfillment of
the requirements for the degree
of
Master of Science in Physics

January 2019

Abstract

As more and more exoplanets have been discovered at a staggering rate, we gradually realised that the population of the exoplanets exhibits a great diversity. We have seen not only the wide-range distribution of the planetary architectures over various parameter spaces, but also specific phenomena that intrigue theorists for a long time, such as Hot Jupiters, large spin-orbit misalignment and free-floating planets. While many models have been proposed to account for these observational facts and some of them can yield very promising results, these theories have not yet been examined in the realistic situation, as their investigations start from either fine-tuned or purely theoretical initial conditions.

In 2015, Atacama Large Millimeter Array changed this picture by releasing the high-resolution image of the HL Tau protoplanetary disk. This image revealed the concentric rings and gaps on the HL Tau disk, which are commonly interpreted as the results of planet formation. Following this assumption, we can extract the configuration of HL Tau system and use that as the initial conditions for planetary evolution to see whether the diverse configurations of the observed planetary systems can be reproduced.

The main objective of this thesis is to investigate the evolution outcomes of the HL Tau system based on initial conditions deduced from the current observation. We first reviewed the basic structure of the protoplanetary disk, the planet-disk interaction, and the observational facts about the HL Tau. We then presented our theoretical methodology and numerical approaches to evolve the HL Tau system. We considered the combined effects of the planetary migration and accretion by adopting the exiting migration theory and modelling the disk structure that hosts multiple planets. We also implemented the migration and accretion model to the N-body numerical simulation framework which was subsequently used for simulations. In total we examined 75 cases of 3-planet system, and each system was evolved for up to 0.1 Gyr after disk dispersal.

We present the results at two different epochs, one at three times the disk lifetime($3\tau_{disk}$) and one at 0.1 Gyr after the disk dispersal. For each epoch, we present the example evolution and explain the pattern that emerged from the plots. We also break down the results in parameter spaces of flaring index, disk lifetime and viscosity. Our main findings include:

1. After $3\tau_{disk}$, the final semi-major axis of planets ranges from 0.007 au to 30 au, while the

planet mass ranges from $0.4\,M_J$ to $10\,M_J$, which is significantly more diverse than the previous study on HL Tau.

2. When the flaring index, disk lifetime and viscosity increase, the final semi-major axis decreases and the final mass increases, and vice versa.
3. All planet systems remain stable up to the simulation time. No instability has been observed.

We also find that all systems survive much longer than the lower limit of instability time predicted from the mutual hill radius, and from which we conclude that the disk-planet interaction at early stage of the planetary evolution can stabilise the system. We further study the stability by investigating the period ratios and the separation between adjacent planets in their mutual hill radius. We find that the migration coupling prevents the planet-pair from entering resonance states smaller than $2:1$ resonance.

Acknowledgements

I would like to express my sincere gratitude to my supervisor, Prof. Yasushi Suto, for his continuous guidance and support during the whole course of my Master programme. From his teaching, I have learned not only the knowledge and techniques that are indispensable for physics research, but also the correct altitude and responsibility that a physics researcher should have, which are invaluable to my future study. Next I would like to thank my principal collaborator, Dr. Kazuhiro Kanagawa, who briefed me on this project with patience and explained many aspects of the protoplanetary disk research with great details. I would also like to thank another collaborator, Toshinori Hayashi, who did the preliminary work with me, contributed to many fruitful discussions and continued encouraging me during the project.

I would like to thank my defence committee members, Prof. Fujihiro Hamba and Prof. Kipp Cannon. Their precious comments are greatly appreciated and play an important role in the later revision of this thesis. I also want to thank other members of UTAP/RESCEU who contributed to the discussions of this project.

Finally I would like to thank my parents who provides me both care and financial support, which I will remember and appreciate for my entire life.

Contents

List of Tables

List of Figures

Chapter 1

Introduction: an Overview

Human beings have a long history of observing planets, which can be traced back to Babylonian period when Mercury, Venus, Mars, Jupiter and Saturn were, for the first time, identified by the ancient astronomers(Sachs, 1974). However, only after the telescope was invented and Newton's law of universal gravitation was formulated, were astronomers able to discover more planets inside the solar system as well as to acquire more details about those planets that had already been identified. The 7th planet Uranus was discovered in 1781 by William Herschel using his own telescope, and then Neptune by Galle in 1846 inspired by the calculation from the French mathematician Le Verrier, marking the culmination of the 19th century's celestial mechanics. As the observation techniques continue to evolve over the years, nowadays we have a repertoire of means to unveil the remaining unknowns of our solar system. For example, in 1970s we sent the Voyagers space probes which visited Jupiter, Saturn and Uranus in succession and then sent back unprecedented in-situ observation data. As similar projects are going to be launched in a steady pace, our solar system will eventually be thoroughly studied in the foreseeable future.

In contrast to the good knowledge that we have on our solar system, our understanding of the exoplanetary systems is just at the very beginning. Though historically many attempts had been made, it was generally believed that there was no confirmed observation until the year of 1992, when the first exoplanet was discovered to be orbiting around the pulsar PSR 1257+12 by analysing the pulsar timing variations(Wolszczan & Frail, 1992). Observing exoplanets via direct imaging is challenging because exoplanets are both tiny compared to the star($\sim 10^{-3}$ in mass ratio) and generally distant from the earth, which are light years away compared to a few AUs for planets in our solar system. Therefore, other supplementary methodologies, such as transit photometry, Doppler spectroscopy(radial velocity) and gravitational micro-lensing, were developed for the sake of more efficient observation. Since the beginning of the 21st century, particularly after the launch of the Kepler space observatory, the number of newly discovered exoplanets per year grows rapidly. Up to now, in total 5,311 exoplanets have been identified, including both confirmed planets and Kepler candidates(Exoplanets.org, 2018).

While the fast-growing number of the exoplanets that had been discovered brought us into a new world never seen before, new intriguing problems also appeared along side with the discoveries. A good example is the Hot Jupiter(HJ), which is a Jupiter-size planet however very close to its hosting star. In 1995, for the first time, a planet orbiting a main-sequence star was detected, namely the 51 Pegasi b. This planet, later considered as a HJ, has a minimum

mass($m \sin i$) $0.46 M_J$ and an orbital period only 4.23 days(Mayor & Queloz, 1995). Later many other HJs were discovered via the radial velocity method, indicating that HJs were not rare in our galaxy. Contrary to the previous understanding of the Jupiter-size planets, the existence of HJ nevertheless challenges the traditional in-situ formation theory of planet, as a contradictorily much larger orbit is necessary to have the sufficient mass-accretion for such a massive planet to form. We may also realise that the formation of HJ is not the only problem that baffles those exoplanet scientists: many related others, such as the large spin-orbit misalignment and number estimate of free floating planets, all remain as open questions. It thus poses a need to find the physical explanations to cater these new discoveries.

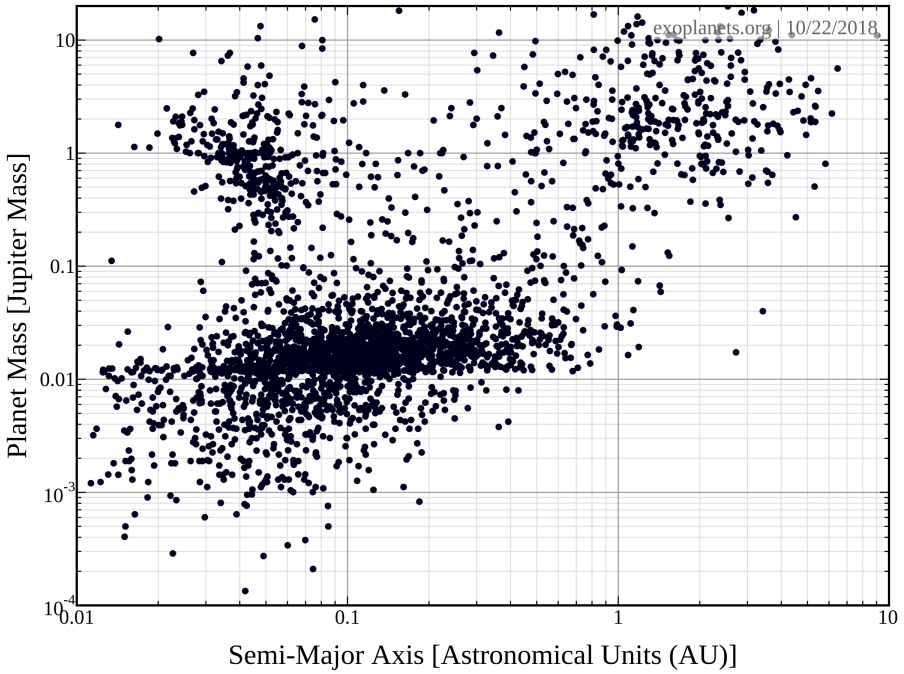

Figure 1.1: Mass against semi-major axis of exoplanets. Exoplanets.org (2018)

Throughout the years, many new insights have been added to the old theoretical framework, which greatly enriched our understanding of the exoplanetary evolution. To reconcile HJ's mass to its position, theorists came out with the Type II disk migration model (e.g., Lin et al., 1996) and later-proposed dynamical evolution model(e.g., Wu & Murray, 2003; Nagasawa et al., 2008). The spin-orbit misalignment may be either due to the famous Kozai mechanism(Kozai, 1962) or the primordial misalignment interpretation due to the binary evolution(Batygin, 2012). While these new theories can partially solve the contradictions, their initial conditions are either fine-tuned to specific purposes or purely theoretical. A new challenge is: "can we find the realistic initial conditions to test the validity of these models?"

Important clues have been brought from the ground-breaking observation of Atacama Large Millimeter Array(ALMA) on the protoplanetary disks. In 2015, the high resolution image(Partnership et al., 2015) on the HL Tau system taken by ALMA revealed the concentric ring and gap structure on the disk, which were commonly interpreted as a result of the gap-opening process due to the formation of planets. If this interpretation is correct, it is possible that we can then extract the initial conditions of the planetary system from the properties of the gaps. Even some parameters like orbital phases cannot be directly inferred from the observation, this discovery can still serve as a strong constraint on the initial conditions. Simbulan et al. (2017) took this idea by connecting the observation on HL Tau disk to the initial planetary configurations and then

evolved the system to Giga-year time-scale. With a particular focus on creating the unstable configurations, their research showed that given the range of parameters that they surveyed, the HL Tau system can produce HJ candidates and planet ejections, as well as diversely-distributed planetary systems.

The pioneering work from Simbulan et al. (2017) is inspiring, and it can be extended further by considering the effects of the planet-disk interactions. Since HL Tau is only one-million-year old and the disk usually has a lifetime of a few million years, we may expect that the migration and accretion will take place for the rest of the disk lifetime, which can further shape the configurations of the planetary system just after the disk dispersal. It is not well understood that whether the combination of migration and accretion will impact on the evolution outcomes of the planetary system, such as the diversity and stability. Based on this motivation, we start this research to investigate on the future of planets emerged from HL Tau in a more realistic physical picture.

This research aims to see if the diverse configurations of the exoplanetary systems can be reproduced using initial conditions deduced from the observed protoplanetary disks, particularly the HL Tau disk. our approach consists of mainly two parts, the disk modelling and simulation. In the disk modelling, we consider the detailed migration and accretion processes of planets inside the disk and also the feedback to the global disk density profile due to individual planet's accretion. In the numerical simulation, we incorporate and implement the planet-disk interactions into the simulation environment and subsequently use the enhanced N-body numerical code to evolve the systems. We analysed the results by showing the patterns emerged, interpreting the physical origins and comparing with the results from other past research. Finally we conclude that to what extent that we can reproduce a diverse population of planetary systems within the range of initial conditions that we survey during the project and what are the impacts of the planet-disk interaction on the final configurations of planetary systems.

We begin by reviewing the protoplanetary disk, the planet-disk interactions and the HL Tau system in Chapter 2, 3, and 4, respectively. In Chapter 5 we explain the methodologies of this research, including both disk modelling and numerical approach. In Chapter 6 we present our discoveries from the numerical simulations and in Chapter 7 we summarise our research and discuss the future work.

Chapter 2

The Protoplanetary Disk

The protoplanetary disk(PPD) is the disk-structured objects that have been observed to be around young stars with a lifetime of a few million years. Commonly recognised as the birthplace for planets, PPD is mainly composed of dust and gas, which structure can be well described by the model based on quasi-equilibrium state. The structure of the PPD strongly shapes the migration and accretion of the planets that form inside the disk; in addition, since the evolution of PPD tightly couples with its structure as well, both the structure and evolution of the disk deserve equal attention while the overall influence on the evolution path of the planet is considered. The review below generally follows the book Armitage (2010) and the review paper Armitage (2015).

2.1 Structure

While considering the structure of the disk, we adopt the approximation that the disk evolves axisymmetrically and slowly enough that the quasi-equilibrium state can be applied at any instant. Starting from the assumptions, we will mainly consider the vertical structure, radial structure and temperature profile of the disk. We use the cylindrical coordinate system (R, z) centered at the star and align the z-direction with the total angular momentum. We define $T(R, z)$, $\Omega(R, z)$ and $\mathbf{v} = (v_R, v_\phi, v_z)$ to be the temperature, angular velocity and velocity of the gas, and use the subscript 'dust' to distinguish the respective quantities that associate with the dust from those that associate with the gas. We also define $\rho(R, z)$ and $\Sigma(R)$ to be the density and surface density. Particularly, the density and surface density of the gas are denoted as ρ_g and Σ_g to avoid any confusion.

2.1.1 Vertical structure

The vertical structure of the PPD can be derived by considering the hydrostatic equilibrium, that is, the balance between the gravitational force exerted by the star and the gas pressure. In order to proceed, three further assumptions have to be introduced:

(i) the disk is vertically isothermal,

(ii) the disk is not self-gravitational, i.e., the disk mass to the stellar mass ratio is much smaller than unity, and

(iii) the disk is geometrically thin.

If we assume irradiation from the star is the only source to heat up the disk, the temperature of the disk is only a function of the cylindrical distance to the star, and thus the first assumption is reasonable. The second assumption ensures that the star is the only source of the gravity which shapes the disk. Finally, the third assumption ensures that the hydrostatic equilibrium is valid as generally pressure inside a disk is small due to the large surface to volume ratio of the disk that favors effective cooling. Therefore, geometrically-thick disks cannot balance the gravity by the gas pressure and only thin disks are relevant to the later discussion.

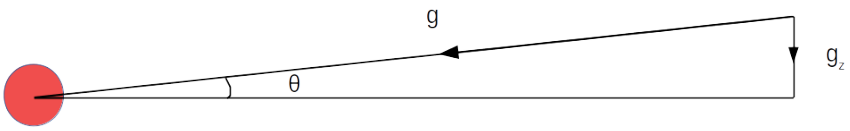

Figure 2.1: Illustration of the basic set-up.

From hydrostatic equilibrium, we can write down the following equation:

$$\begin{aligned}\frac{1}{\rho_g}\frac{dP}{dz} &= \frac{-\mathcal{G}M_*}{R^2+z^2}\sin\theta,\\ \frac{dP}{dz} &= \frac{-\mathcal{G}M_*}{R^2+z^2}\frac{z}{(R^2+z^2)^{1/2}},\rho_g\\ &= \frac{-\mathcal{G}M_* z}{(R^2+z^2)^{3/2}}\rho_g,\end{aligned} \tag{2.1}$$

where $\mathcal{G}$ is the gravitational constant, P is the gas pressure, and M_* is the mass of the star. From the isothermal equation of state, we have $P = \rho_g c_s^2$, where c_s is the sound speed. Substituting to equation (2.1), one obtains

$$c_s^2\frac{d\rho_g}{dz} = \frac{-\mathcal{G}M_* z}{(R^2+z^2)^{3/2}}\rho_g. \tag{2.2}$$

$$\tag{2.3}$$

Equation (2.2) can be integrated to give

$$\rho_g = \rho_{g,0}\exp\left[\frac{\mathcal{G}M_*}{c_s^2(R^2+z^2)^{1/2}}\right]. \tag{2.4}$$

Consider the case when $z \ll R$. Given the Keplerian orbital velocity at the mid-plane $\Omega_K \equiv \sqrt{\mathcal{G}M_*/R^3}$, We define h as the scale height that takes the form

$$h \equiv \frac{c_s}{\Omega_K}. \tag{2.5}$$

Equation 2.4 can then be re-expressed as

$$\rho_g = \rho_{g,0} \exp\left(-z^2/2h^2\right), \tag{2.6}$$

and $\rho_{g,0}$ is the gas density at the mid-plane. Further we can write the mid-planet surface density as $\Sigma_g = \int_{+\infty}^{-\infty} \rho dz$ and obtain the following relation for $\rho_{g,0}$ and Σ_g:

$$\rho_{g,0} = \frac{1}{\sqrt{2\pi}} \frac{\Sigma_g}{h}. \tag{2.7}$$

Equation (2.6) shows that the vertical density profile follows the Gaussian distribution. At a range where z/h is around unity, even the full treatment which does not assume condition $z \ll R$ produces a density ρ_g that only deviates slightly from the Gaussian profile. Although there exist other factors which can cause significant deviation from the Gaussian profile, such as the non-isothermal temperature profile, magnetic pressure(e.g Hirose & Turner (2011)), etc., the detailed discussion of these effects is beyond the scope of this review.

2.1.2 Radial Structure

Compared to the relatively trivial derivation of the vertical density profile, the radial density profile of the disk involves detailed considerations of the transport of the angular momentum and therefore will be discussed later in Section 2.2. Nevertheless, when the surface density Σ_g and temperature T distribution are known, the orbital velocity of the gas $v_{\phi,gas}$ at the mid-planet can be derived from the Euler equation by considering force balance in the radial direction

$$\frac{\partial \mathbf{v}}{\partial t} + (\mathbf{v} \cdot \nabla)\mathbf{v} = \frac{1}{\rho_g} \nabla P - \nabla \Phi, \tag{2.8}$$

where ϕ is the gravitational potential. Since we are interested in the steady state of the disk, $\partial/\partial t \equiv 0$. Taking only the radial component of equation (2.8), we have

$$\frac{v_\phi^2}{R} = \frac{\mathcal{G} M_*}{R^2} + \frac{1}{\rho_g} \frac{dP}{dR}. \tag{2.9}$$

Assuming $\Sigma_g \propto R^\gamma$ and $T \propto R^\beta$ and using the relations:

$$c_s^2 \propto T, \tag{2.10}$$

$$\rho_g \propto \frac{\Sigma_g}{h}, \tag{2.11}$$

we get

$$P \propto R^{\gamma - \frac{3-\beta}{2}} \propto R^n, \tag{2.12}$$

where we define $n \equiv \gamma - \frac{3-\beta}{2}$. Substitute the expression of P into equation 2.9 and define the mid-planet Keplerian speed as $v_K \equiv \Omega_K R \equiv \sqrt{\mathcal{G} M_*/R}$, the final result is

$$\frac{v_\phi^2}{R} = \frac{v_K^2}{R} + \frac{c_s^2}{P} \frac{dP}{dR}, \tag{2.13}$$

Hence, we can obtain v_ϕ as

$$\begin{aligned} v_\phi &= v_K \left[1 + n\frac{c_s^2}{v_K^2}\right]^{1/2}, \\ &= v_K \left[1 + n\left(\frac{h}{R}\right)^2\right]^{1/2}. \end{aligned} \tag{2.14}$$

It can be concluded here that the difference between the gas speed v_ϕ and Keplerian speed v_K is in the order of square of h/R. Although this deviation is only a tiny fraction of the Keplerian speed(for example, when $n = -3$ and $[h/R]_{R=1\,\mathrm{au}} = 0.05$, the fractional difference $(v_K - v_\phi)/v_K$ is 0.4 %), this difference is vitally important in considering the growth of particles inside the disk: since large particles orbit at Keplerian speed, they will experience a headwind while moving inside the sub-Keplerian disk, therefore losing angular momentum due to the viscous drag and moving inwards in a spiral.

The above derivation only considers the Keplerian speed deviation at the mid-plane. More detailed treatment, provided by Takeuchi & Lin (2002), also includes the vertical dependence. Using the same set-up, their result gives

$$\Omega \approx \Omega_K \left[1 + \frac{1}{4}\left(\frac{h}{R}\right)^2 \left(\beta + 2\gamma - 3 + \beta\frac{z^2}{h^2}\right)\right], \tag{2.15}$$

Considering the off-plane Keplerian orbital velocity $\Omega_{K,z}$ written as a function of z:

$$\begin{aligned} \Omega_{K,z} &= \left[\frac{\mathcal{G}M_*}{(R^2+z^2)^{3/2}}\right]^{1/2}, \\ &= \left(\frac{\mathcal{G}M_*}{R^3}\right)^{1/2} \left[1 + \left(\frac{z}{R}\right)^2\right]^{-3/4}, \\ &\approx \Omega_K \left[1 - \frac{3}{4}\left(\frac{z}{R}\right)^2\right]. \end{aligned} \tag{2.16}$$

Therefore, to the first order to $(z/R)^2$, we obtain

$$\Omega - \Omega_{K,z} \approx \frac{1}{4}\left(\frac{h}{R}\right)^2 \Omega_K \left[\beta + 2\gamma - 3 + (\beta+3)\left(\frac{z}{h}\right)^2\right]. \tag{2.17}$$

Choosing typical values as $\beta = -0.5$ and $\gamma = -1$, when $\Omega - \Omega_{K,z} = 0$, we have

$$\frac{z}{h}\Big|_{\Omega=\Omega_K} \sim 1.48.$$

The result shows that near the mid-plane region below $z \sim 1.48h$, particles rotate faster than the gas and therefore experience a headwind; otherwise, particles rotate slower than the gas.

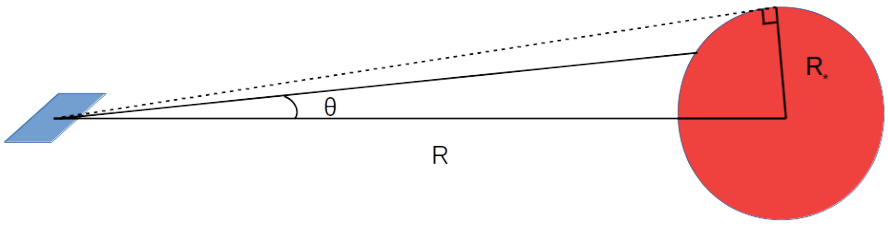

Figure 2.2: Illustration of the flux from the star.

2.1.3 Temperature Profile

To investigate the temperature profile of the PPD, one may assume that the PPD is in thermal equilibrium, and what remains is to find the temperature at which the energy gain and loss balance out each other. There are mainly two sources that the PPD can gain thermal energy from: the irradiation from its hosting star and the gravitational energy released by the accretion matter. On the other hand, the PPD also loses energy through re-emission process. In the following derivation we will start from a simplified disk model, which is the razor-thin and passive disk. If the disk energy income can be solely determined by the irradiation from the hosting star, the disk is called "passive" and thus the temperature profile will be determined by its geometrical shape. A razor-thin disk will then ensure that the mid-plane of the disk intercept all the radiation and then re-emit in black body spectrum.

Consider a star in radius R_* with a constant stellar surface brightness I_*. Let θ and ϕ be the polar and azimuthal angles. If we write the unit vector $\hat{\mathbf{n}}$ of the light direction as $(\sin\theta\cos\phi, \sin\theta\sin\phi, \cos\theta)$, then the light flux F can be expressed as

$$\begin{aligned} F &= \int I_*(\hat{\mathbf{n}}\cdot\hat{\mathbf{x}})d\Omega \\ &= \int I_* \sin^2\theta\cos\phi d\theta d\phi. \end{aligned} \tag{2.18}$$

Since only half of the star can contribute to the total flux, equation (2.18) is integrated over $0 < \theta < \sin^{-1}\left(\frac{R_*}{R}\right)$ and $-\pi/2 < \phi < \pi/2$ and we obtain

$$\begin{aligned} F &= I_* \int_{-\pi/2}^{\pi/2} \cos\phi d\phi \int_0^{\sin^{-1}(R_*/R)} \sin^2\theta d\theta \\ &= 2I_* \left[\frac{1}{2} - \frac{1}{4}\sin 2\theta\right]_0^{\sin^{-1}(R_*/R)} \\ &= I_* \left[\sin^{-1}\left(\frac{R_*}{R}\right) - \frac{R_*}{R}\sqrt{1-\left(\frac{R_*}{R}\right)^2}\right]. \end{aligned} \tag{2.19}$$

The brightness of the star at its surface can be related to the effective temperature of the starby using the Stefan-Boltzmann law (Rybicki & Lightman, 1979)

$$I_* = \frac{F}{\pi} = \frac{\sigma T_*^4}{\pi}. \tag{2.20}$$

For one side of the disk, the flux $F = \sigma T^4$. Substituting back to both sides of the equation (2.19) gives

$$\left(\frac{T}{T_*}\right)^4 = \frac{1}{\pi}\left[\sin^{-1}\left(\frac{R_*}{R}\right) - \frac{R_*}{R}\sqrt{1-\left(\frac{R_*}{R}\right)^2}\right]. \tag{2.21}$$

In the region far from the star, i.e., $R_* \ll R$, equation (2.21) is reduced to a simple power law temperature profile

$$T \propto R^{-3/4}. \tag{2.22}$$

Using the relation $c_s^2 \propto T$ and $h \equiv c_s/\Omega_K$, the aspect ratio is

$$\frac{h}{R} \propto R^{-\frac{3}{4}\cdot\frac{1}{2}+\frac{3}{2}-1} \propto R^{1/8}. \tag{2.23}$$

Defining the flaring index f through $(h/R) \propto R^f$, the temperature profile for a razor-thin, passive disk gives $f = 0.125$. This shows that when R increases, the aspect ratio also increases, resulting in a disk which is called 'flared'.

Flared disk

We note that the above result is over-simplified in many aspects. At large R, the flared part of the disk contributes to additional absorption area and therefore gaining higher temperature than the originally-assumed razor-thin disk. The full solution that takes account of the flaring effect can be derived in a similar way, but a simplified consideration that takes the limit $R_* \ll R$ and the star to be a point source is sufficient to understand the effect qualitatively.

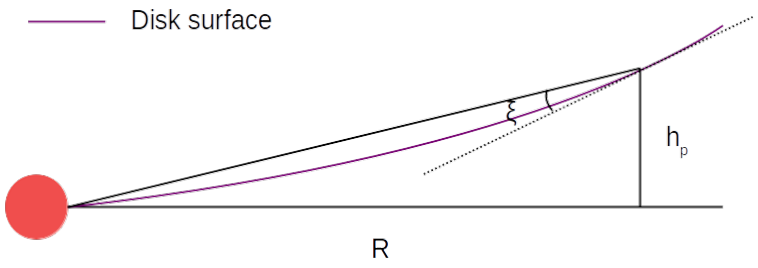

Figure 2.3: Illustration of a flared disk.

Following the arguments in Armitage (2010), we define a maximum absorption height h_p at radius R and then define ξ as the angle between the incoming radiation and the tangent of the local disk surface:

$$\xi \equiv \frac{dh_p}{dR} - \frac{h_p}{R}. \tag{2.24}$$

ξ is determined by the relation between h_p and scale height h. Assuming black-body emission,

we can equate the local heating rate(left-side) and the cooling rate(right-side) as

$$\xi \left(\frac{L_*}{4\pi R^2} \right) = \sigma T^4. \tag{2.25}$$

Using $L_* = 4\pi R_*^2 \sigma T_*^4$, we obtain

$$\left(\frac{T}{T_*} \right)^4 = \xi \left(\frac{R_*}{R} \right)^2, \tag{2.26}$$

$$T \propto \xi^{1/4} R^{-1/2}. \tag{2.27}$$

This shows that at large radii the temperature of a flared disk drops slower than that of a razor-thin disk, as R increases(c.f. equation (2.23)).

So far we also only consider a single-composition model of the disk, where in reality the dust dominates the absorption inside the disk and thus its radiative thermal properties have to be taken care of. We define the ϵ as the efficiency of emission/absorption of dust relative to the black-body. When the wavelength of the incoming radiation is smaller than the radius of the dust, the dust absorbs and emits like a blackbody with emissivity $\epsilon = 1$; when the wavelength is longer than the dust radius, the dust emissivity drops with $\epsilon \propto \lambda^{-1}$. Using the same thermal equilibrium argument, the dust temperature T_{dust} can be expressed as

$$\begin{aligned} \frac{T_{dust}}{T_*} &= \left(\frac{\epsilon_*}{\epsilon_{dust}} \right)^{1/4} \left(\frac{R_*}{2R} \right)^{1/2} \\ &= \left(\frac{T_{dust}}{T_*} \right)^{1/4} \left(\frac{R_*}{2R} \right)^{1/2}, \\ \Rightarrow \frac{T_{dust}}{T_*} &= \left(\frac{R_*}{2R} \right)^{2/5} \propto R^{-2/5}, \end{aligned} \tag{2.28}$$

where ϵ_{dust} is the weighted emissivity of the dust averaged over the dust thermal emission, and ϵ_* is the weighted emissivity for the absorption averaged over the stellar spectrum. The above analysis follows the two-layer model developed by Chiang & Goldreich (1997). For a star with $0.5\,\mathrm{M}_\odot$ mass, $2.5\,\mathrm{R}_\odot$ radius and 4000 K effective temperature, the dust temperature profile is

$$T_{dust} = 550 \left(\frac{R}{1\,\mathrm{au}} \right)^{-2/5} \mathrm{K}. \tag{2.29}$$

2.2 Evolution

The PPD evolves as the gas keeps accreting onto the central star, whereas the disk wind launched by the magnetic field and photoevaporation effect continues to cause the mass loss. The movement of the gas is governed by the gain and loss of the angular momentum. Therefore, the key idea to understand the evolution of the PPD is to understand how the angular momentum is transferred and redistributed within the disk. Starting from the basic conservation laws, we can write the hydrodynamical equations in the context of the PPD and then obtain various characteristics of the disk evolution. The following review mainly follows Pringle (1981).

2.2.1 Classical Picture

The classical picture of the disk evolution concerns the evolution of a vicious, axisymmetric and geometrically-thin disk. Construct the cylindrical coordinate system (R, z) as before, the conservation of mass and angular momentum can be written as

$$R\frac{\partial \Sigma_g}{\partial t} + \frac{\partial}{\partial R}(R\Sigma_g v_R) = 0 \tag{2.30}$$

$$R\frac{\partial}{\partial t}(R^2\Omega\Sigma_g) + \frac{\partial}{\partial R}(R^2\Omega \cdot R\Sigma_g v_R) = \frac{1}{2\pi}\frac{\partial G}{\partial R}. \tag{2.31}$$

Compared with equation (2.8), equation (2.31) is derived from the Navier-Stokes equation which also takes account of the viscosity. G on the right side of the equation (2.31) is the vicious torque that acting on the edge of the annulus:

$$G = 2\pi R \cdot \nu\Sigma_g R\frac{d\Omega}{dR} \cdot R, \tag{2.32}$$

where ν is the kinematic viscosity. From equation (2.30) we have

$$\frac{\partial \Sigma_g}{\partial t} = -\frac{1}{R}\frac{\partial}{\partial R}(R\Sigma_g v_R). \tag{2.33}$$

Substituting equations (2.33) and (2.32) to equation (2.31) and use prime to denote $\frac{d}{dR}$, then

$$-R^2\Omega\frac{\partial}{\partial R}(R\Sigma_g v_R) + R\Sigma_g\frac{\partial}{\partial t}(R^2\Omega) + \frac{\partial}{\partial R}(R^2\Omega \cdot R\Sigma_g v_R) = \frac{\partial G}{\partial R}, \tag{2.34}$$

$$R\Sigma_g\frac{\partial}{\partial t}(R^2\Omega) + R\Sigma_g v_R\frac{\partial}{\partial R}(R^2\Omega) = \frac{\partial}{\partial R}(v\Sigma_g R^3\Omega'). \tag{2.35}$$

Since $\frac{d}{dt} \equiv \frac{\partial}{\partial t} + v_R\frac{\partial}{\partial R}$,

$$R\Sigma_g\frac{dR}{dt}(R^2\Omega)' = \frac{\partial}{\partial R}(v\Sigma_g R^3\Omega'), \tag{2.36}$$

$$R\Sigma_g v_R = \frac{1}{(R^2\Omega)'}\frac{\partial}{\partial R}(v\Sigma_g R^3\Omega'). \tag{2.37}$$

Substituting equation (2.37) back to equation (2.33),

$$\frac{\partial \Sigma_g}{\partial t} = -\frac{1}{R}\frac{\partial}{\partial R}\left[\frac{1}{(R^2\Omega)'}\frac{\partial}{\partial R}(v\Sigma_g R^3\Omega')\right]. \tag{2.38}$$

Using Keplerian $\Omega \propto R^{-3/2}$,

$$\frac{\partial \Sigma_g}{\partial t} = \frac{3}{R}\frac{\partial}{\partial R}\left[R^{1/2}\frac{\partial}{\partial R}(v\Sigma_g R^{1/2})\right], \tag{2.39}$$

and the radial velocity is given by

$$v_R = -\frac{3}{\Sigma_g R^{1/2}}\frac{\partial}{\partial R}\left(\nu\Sigma_g R^{1/2}\right). \tag{2.40}$$

The above result describes the diffusion of the gas. Additional terms need to be considered if other sources of mass loss(e.g. thermal wind) or external torques are present. In the case of the extra mass loss $\dot{\Sigma}_{g_{ext}}$, equation (2.39) simply becomes

$$\frac{\partial \Sigma_g}{\partial t} = \frac{3}{R}\frac{\partial}{\partial R}\left[R^{1/2}\frac{\partial}{\partial R}(\upsilon \Sigma_g R^{1/2})\right] + \dot{\Sigma}_{g_{ext}}. \tag{2.41}$$

With the presence of the radial flow v_{ext} driven by external torque, it becomes

$$\frac{\partial \Sigma_g}{\partial t} = \frac{3}{R}\frac{\partial}{\partial R}\left[R^{1/2}\frac{\partial}{\partial R}(\upsilon \Sigma_g R^{1/2})\right] - \frac{1}{R}\frac{\partial}{\partial R}(R\Sigma_g v_{ext}). \tag{2.42}$$

We can define a new set of variables

$$X \equiv 2R^{1/2}, \tag{2.43}$$

$$f \equiv \frac{3}{2}\Sigma_g X, \tag{2.44}$$

to write equation (2.39) in a more enlightening way:

$$\frac{2}{3}\frac{\partial}{\partial t}\left(\frac{f}{X}\right) = 3\left(\frac{2}{X}\right)^2 \frac{2}{X}\frac{\partial}{\partial X}\left[\frac{X}{2}\frac{2}{X}\frac{\partial}{\partial X}(\nu f/3)\right]. \tag{2.45}$$

Then trivial calculations give

$$\frac{\partial f}{\partial t} = \frac{12\nu}{X^2}\frac{\partial f^2}{\partial X^2}, \tag{2.46}$$

which is a diffusion equation with a diffusion coefficient $12\nu/X^2$. If a disk has a characteristic scale of ΔR, the diffusion time scale can be written as

$$\tau_\nu \sim \frac{(\Delta X)^2}{D} \sim \frac{(\Delta R)^2}{\nu}. \tag{2.47}$$

2.2.2 Solutions of the surface density Σ_g

Consider the steady-state of equations (2.30) and (2.31) as well as equation (2.32), then the time derivative will vanish and we obtain:

$$2\pi R\Sigma_g \upsilon_R \cdot R^2\Omega = 2\pi R^3 \nu \Sigma_g \frac{d\Omega}{dR} + C \tag{2.48}$$

where C is a constant of integration. The left-hand side of the equation can be re-expressed by realising that the accretion rate $\dot{M}$ is equal to $-2\pi R\Sigma_g \upsilon_R$:

$$-\dot{M}R^2\Omega = 2\pi R^3 \nu \Sigma_g \frac{d\Omega}{dR} + C. \tag{2.49}$$

To determine the value of the constant C, the boundary condition of Ω is needed. When $R = R_*$, i.e., at the surface of the star, the angular frequency Ω of the disk should be equal to that of the star Ω_*. In the region where $R \gg R_*$, Ω can be approximated by the Keplerian

angular frequency $\Omega_K \propto R^{-3/2}$. Due to the discrepancy between Ω_* and Ω_K, it is expected that there must be a point at some R' where the viscous stress vanishes or $d\Omega/dR = 0$. In general R' is very close to R_*, and using this approximation, the value of C is

$$C \approx -\dot{M} R_*^2 \Omega_*. \tag{2.50}$$

Substituting the equation (2.50)to equation (2.49) at the region where $\Omega \propto R^{-3/2}$, we have

$$-\dot{M} R^2 \Omega = 2\pi R^3 \nu \Sigma_g \frac{d\Omega}{dR} - \dot{M} R_*^2 \Omega_*, \tag{2.51}$$

$$3\pi R^2 \Omega (\nu \Sigma_g) = \dot{M} \left(R^2 \Omega - R_*^2 \Omega_* \right), \tag{2.52}$$

$$\nu \Sigma_g = \frac{\dot{M}}{3\pi} \left(1 - \sqrt{\frac{R_*}{R}} \right). \tag{2.53}$$

If the region $R \gg R_*$ is considered, equation (2.53) becomes

$$\Sigma_g \approx \frac{\dot{M}}{3\pi\nu}. \tag{2.54}$$

This is the steady state solution of the surface density at large radii.

2.2.3 Viscosity and the Shakura-Sunyeav α prescription

We may realise that the viscosity plays a central role in the angular momentum transport that takes place inside the disk, and thus it is important to understand the physics that contributes to the viscosity. One might think that the molecular collision is one of the sources. Denote such viscosity as ν_m, then ν_m is approximately given by λc_s, where λ is the mean free path and c_s is the sound speed. Since $\lambda = (n\sigma_m)^{-1}$, where n is the density and σ_m is the cross-section, if typical values $\sigma_m \approx 2 \times 10^{-15}\,\mathrm{cm}^2$ and $n = 10^{12}\,\mathrm{cm}^{-3}$ are used for $R = 10\,\mathrm{au}$, the viscous time scale given by equation (2.47) is

$$\tau_\nu \sim O(10^{13})\mathrm{yr}. \tag{2.55}$$

This time-scale is much longer than the lifetime of the protoplanetary disk, so the molecular viscosity alone cannot explain the total viscosity required.

It is widely recognised that the turbulence caused by the instabilities makes the major contribution to the viscosity, and to characterise it, we follow the prescription introduced by the paper Shakura & Sunyaev (1973), and define the dimensionless α parameter

$$\nu = \alpha c_s h. \tag{2.56}$$

It is possible to assume that the value of α is a constant, and by taking the power-law profile of the temperature $T \propto R^\beta$, the kinematic viscosity ν can be expressed as $\nu \propto r^\gamma$, where $\gamma = \beta + 3/2$.

2.2.4 Stability of the disk

It is obvious that the disk is not guaranteed to be stable for arbitrary values of the parameters; to remain in a stable state, the PPD is subjected to various stability criteria. The Rayleigh criterion(e.g.Pringle & King (2007)) that describes the linear stability of the shear flow requires

$$\frac{d}{dR}(R^2\Omega) > 0, \tag{2.57}$$

which is trivially satisfied in the context of the PPD, since the specific angular momentum $R^2\Omega_K$ always follows this criterion. There are many other factors to consider, and due to the limitation of this paper, only the self-gravity will be discussed in detail here, while some of the others will only be briefly mentioned.

When the disk is considered as self-gravitating, not only the gravitational force from the central star but also the gravitational force between the disk elements have to be taken account of. A formal discussion of this instability can be found in Toomre (1964), in which the criterion of the self-gravitating disk is described by Toomre's Q parameter:

$$Q \equiv \frac{c_s\Omega}{\pi\mathcal{G}\Sigma_g}. \tag{2.58}$$

For a disk to be gravitational stable, its Q value should be less than a critical value $Q_{crit} \sim 1$. Using the profile derived for the steady-state given by equation (2.54), the expression of Q can be re-written as

$$Q = \frac{3\nu c_s\Omega}{\mathcal{G}\dot{M}} = \frac{3\alpha c_s^3}{\mathcal{G}\dot{M}}. \tag{2.59}$$

It is a reasonable assumption that both α and accretion rate $\dot{M}$ are approximately constant, therefore the Q value in this context is a function of c_s only. Since that $c_s^2 \propto T$, the disk will become gravitationally unstable when its temperature drops below a certain critical value. From the disk mass point of view, equation (2.58) can also be written in terms of the total mass of the disk $M_{disk} \sim \pi R^2\Sigma$

$$Q \sim \frac{c_s\Omega_K\pi R^2}{\pi\mathcal{G}M_{disk}} \cdot \frac{M_*}{M_*} = \frac{c_s\Omega_K}{\Omega_K^2 R} \cdot \frac{M_*}{M_{disk}} = \frac{h}{R} \cdot \frac{M_*}{M_{disk}}. \tag{2.60}$$

So the instability criterion becomes

$$\frac{h}{R} < \frac{M_{disk}}{M_*}. \tag{2.61}$$

To the same order of magnitude of the aspect ratio, this criterion agrees with the rough analysis which considers the condition when the gravitational field strength created by the disk is comparable to that fo the star. Using the typical values of the aspect ratio $h/r \sim 0.05$ and star mass $M_* = 1\,\mathrm{M}_\odot$, the critical disk mass is around $0.05\,\mathrm{M}_\odot$. Gravitational instability can lead to fragmentation, which is thought to be one of the channels for the formation giant planet.

Under the presence of the magnetic field, magnetorotational instability(MRI) may arise. The process that how this instability occurs is illustrated by Figure 2.4. Consider the vicinity of the point at a distance R co-rotating with the star, with two point masses well-coupled with the magnetic field. Under the perturbation, the two masses are then separated radially, and due to the Keplerian motion radial displacement causes subsequent angular separation. The

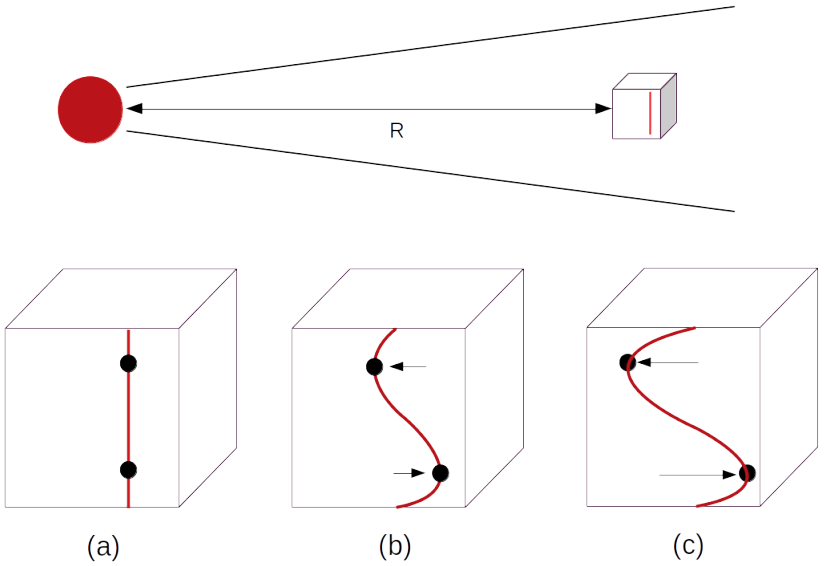

Figure 2.4: Illustration of the magnetorotational instability(MRI). (a) initially unperturbed state; (b) perturbation causes small radial displacement, resulting in angular displacement; (c) magnetic tension removes the angular momentum and further separates two elements.

magnetic tension then acts on and transfers angular momentum from the inner mass element to the outer one, which further enhances the radial displacement and lead to instability. Detailed magnetohydrodynamical(MHD) calculation and stability analysis showed that given any power-law angular velocity $\Omega \propto R^{-q}$, if the condition $q > 0$ is fulfilled, arbitrarily weak magnetic field can still induce this instability.

Other instabilities, such as purely hydrodynamical instability and shear instability, are also important in generation of turbulence and structure formation. The situation will be further complicated if solid is present and couples with the gas, while additional channel of instability, e.g. streaming instability, may emerge as a result of the angular momentum exchange between solid and gas.

2.2.5 Disk Dispersal

The total mass of the PPD is obviously not conserved: during the disk evolution the PPD continuously loses mass and eventually enters the gas-free stage after most of the gas is lost. The dominant channel of mass loss is the gas accretion onto the star. Taking the accretion rate to be the median of the observed value, which is $10^{-8}\,\mathrm{M_\odot yr^{-1}}$, one can estimate that the disk has a lifetime in the order of million year. However, if the accretion is the only channel that contributes to the mass loss, the discrepancy between the theory and observation arises as the mass loss rate will be too low at the final stage of the disk. This contradicts the fact that disks in such stages have not been observed(Alexander et al., 2013). It is then reasonable to consider other means of mass removal which can produce a sharp cut-off of surface density evolution rather than a tail. Based on this motivation, the two main candidates for mass loss are the photoevaporation and MHD winds.

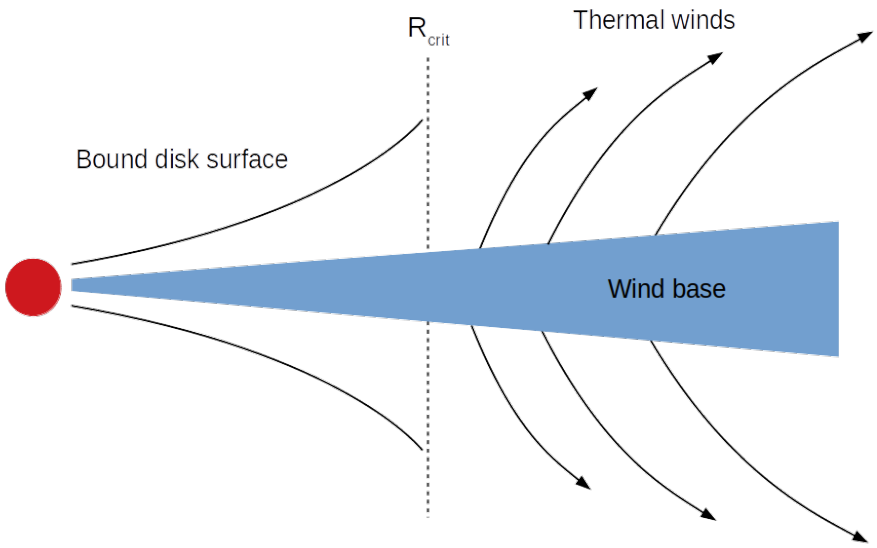

Figure 2.5: Illustration of the thermal winds launched due to photoevaporation.

Photoevaporation

Mass loss due to photoevaporation is caused by the thermal winds launched from the surface of the disk. The high-energy photons from the star or other sources can ionise the molecule on the surface of the disk and raise the temperature. When the thermal energy of the particle exceeds the gravitational potential energy, the particle will no longer remain bounded, resulting in thermal winds that carry matter away. To understand this effect quantitatively, we define a critical distance R_{crit} at which the gas particle is able to escape. Careful calculations considering wind structure and rotation show that

$$R_{crit} \approx 0.2 R_{\rm grav}, \tag{2.62}$$

where

$$R_{\rm grav} = \frac{\mathcal{G} M_*}{c_s^2} \tag{2.63}$$

is the distance when the thermal energy $k_B T$ is equal to the gravitational energy, and c_s is the sound speed of the gas. Figure 2.5 shows the illustrative picture of photoevaporation. Within the critical radius, the gas is bounded by the flared disk surface; beyond the critical radius, thermal winds were launched from the base, which carry away the mass at around sound speed. The mass loss rate per unit area, $\dot{\Sigma}_{\rm evap}$, can thus be expressed as

$$\dot{\Sigma}_{\rm evap} \approx 2 \mu m_H n_0 c_s, \tag{2.64}$$

where μ is the mean molecular weight, n_0 is the number density at the base and is a function of distance R. Generally solving the radiative transfer equation is required to obtain $n_0(R)$. The mass loss rate can then be trivially obtained by integrating equation (2.64) over the inner

radius R_{in} to the outer radius of the disk R_{out}:

$$\dot{M}_{\rm evap} = \int_{R_{in}}^{R_{out}} 2\pi R \dot{\Sigma}_{\rm evap} dR. \tag{2.65}$$

The photoevaporation effect obviously depends on the energy of the photons, and the above analysis is mainly valid in the case of the extreme ultraviolet(EUV) photon. Under the flux of EUV photon, there will be a sharp ionising front separating the heated layer and the remaining cool part of the disk. In the case of the X-ray and far ultraviolet photons, the sharp front is absent, making the analytical modelling even harder. Given the flux of EUV to be ϕ, the mass loss rate estimated by Font et al. (2004) is

$$\dot{M}_{\rm evap} \approx 1.6 \times 10^{-10} \left(\frac{M_*}{\rm M_\odot}\right)^{1/2} \left(\frac{\phi}{10^{41}\,\rm s^{-1}}\right)^{1/2} \rm M_\odot yr^{-1}. \tag{2.66}$$

MHD Wind

The MHD wind is an alternative source of the mass loss, which can be launched by the magneto-centrifugal driving force in the presence of the magnetic field lines. To understand this effect, we can first write down the Lorentz force per unit volume as

$$\frac{\mathbf{J} \times \mathbf{B}}{c} = -\nabla \left(\frac{B^2}{8\pi}\right) + \frac{\mathbf{B} \cdot \nabla \mathbf{B}}{4\pi}. \tag{2.67}$$

Here $\mathbf{J}$ is the current density and $\mathbf{B}$ is the magnetic field. The first and second terms on the right-hand side are the magnetic pressure and tension, respectively. In the region close to the mid-plane of the disk, i.e., $z \ll h$ where z is the height, the thermal pressure $\rho_g c_s^2$ is larger than the magnetic pressure $B^2/8\pi$; however, as z increases thermal pressure drops due to decrease in density, where magnetic pressure stays almost constant due to conservation of flux. Therefore, beyond a certain height the magnetic pressure will dominate over the thermal pressure and the wind is launched. The wind is then supported by the field line until the Alfvén surface is reached, where kinetic energy density $\rho_g v^2$ surpasses the magnetic energy density. Beyond this boundary the wind will be strong enough to bend the field lines. Between where the wind is launched and the Alfvén surface, the acceleration due to magnetic field is assumed to be nearly zero, which means $\mathbf{J} \times \mathbf{B} \approx 0$. This region is called the force-free region.

Compared to the thermal wind driven by photoevaporation, MHD wind depends only on the magnetic flux and thus can be launched at even very inner part of the disk, since it is not constrained by the star's potential. The investigation on the coupling between these two effects remains as an open question; nevertheless in reality the disk winds are more likely to be driven by both the photoevaporation and MHD effect.

Chapter 3

Planetary Migration

A planet is never an isolated object: along its evolution history it keeps interacting gravitationally with its surroundings, including the PPD where it was born and the star that it was bound to. In this chapter we will review the various interactions between the planet and its surrounds, mainly the planet-disk interaction. This review basically follows Armitage (2010). When a planet is embedded in a PPD, it keeps exchanging of the angular momentum via gravitational torques and, as a result, migrates. This is called the planetary migration. The planetary migration is particularly important in considering the early evolution phase of a planetary system as it can significant change the planetary configuration in a short time-scale. Modelling the planetary migration requires the quantitative understanding the physical origins of the torques arising from the non-axisymmetric structure of the disk. Here we follow the treatment of Goldreich & Tremaine (1979), which approached this problem by considering the linear perturbation of the gravitational potential followed by the responses of the disk in different resonant modes.

3.1 The Resonant Torques

Using the same mathematical formalism as Goldreich & Tremaine (1979), we use the cylindrical coordinate system (R, θ, z). Let $\mathbf{v}_0 = R\Omega\hat{\mathbf{e}}_\theta$ and σ_0 be the unperturbed azimuthal velocity and surface density, while $\mathbf{v}_1$ and σ_1 are the first order perturbations of the respective quantity. We introduce an external perturbation potential $\psi_1(R, \theta, t)$ and denote the additional potential perturbation due to σ_1 as ψ_1^D. The linearised hydrodynamical perturbation equations then reduce to

$$\frac{\partial \mathbf{v}_1}{\partial t} + (\mathbf{v}_0 \cdot \nabla)\mathbf{v}_1 + (\mathbf{v}_1 \cdot \nabla)\mathbf{v}_0 = -\nabla(\psi_1 + \psi_1^D + \eta_1), \tag{3.1}$$

$$\frac{\partial \sigma_1}{\partial t} + \nabla \cdot (\sigma_0 \mathbf{v}_1) + \nabla \cdot (\sigma_1 \mathbf{v}_0) = 0, \tag{3.2}$$

where

$$\eta_1 = c_{s0}^2 \left(\frac{\sigma_1}{\sigma_0}\right), \tag{3.3}$$

$$\nabla^2 \psi_1^D = 4\pi \mathcal{G} \sigma_1 \delta(z). \tag{3.4}$$

Here c_{s0} is the unperturbed sound speed, $\delta(z)$ is the Dirac delta function, and η is the enthalpy related to the sound speed. Equations (3.1) and (3.2) are derived from the angular momentum conservation and mass conservation, respectively. Then by writing each perturbation variable in the form of $\mathbf{X} = \mathbf{X}(R) \exp i(m\theta - \omega t)$ with m being an integer, the momentum conservation can be re-written as

$$i(m\Omega - \omega) v_{1,R} - 2\Omega v_{1,\theta} = -\frac{d}{dR}(\psi_1 + \psi_1^D + \eta_1), \tag{3.5}$$

$$2B v_{1,R} + i(m\Omega - \omega) v_{1,\theta} = -\frac{im}{R}(\psi_1 + \psi_1^D + \eta_1), \tag{3.6}$$

where $v_{1,R}$ and $v_{1,\theta}$ are $\hat{\mathbf{R}}$ and $\hat{\theta}$ components of $\mathbf{v}_1$. B is the Oort parameter defined as

$$B(R) = \Omega(R) + \frac{R}{2}\frac{d\Omega}{dR}, \tag{3.7}$$

Solving $v_{1,R}$ and $v_{1,\theta}$ from the above equations, we obtain

$$v_{1,R} = -\frac{i}{D}\left[(m\Omega - \omega)\frac{d}{dR} + \frac{2m\Omega}{R}\right](\psi_1 + \psi_1^D + \eta_1), \tag{3.8}$$

$$v_{1,\theta} = \frac{1}{D}\left[2B\frac{d}{dR} + \frac{m}{R}(m\Omega - \omega)\right](\psi_1 + \psi_1^D + \eta_1), \tag{3.9}$$

$$D = \kappa^2 - (m\Omega - \omega)^2, \tag{3.10}$$

where $\kappa = 2\sqrt{B(R)\Omega(R)}$ is the epicyclic frequency. We can then substitute the above solution to the mass conservation equation, and the resulting differential equation shows that there will be singularities at both $m\Omega - \omega = 0$ and $D = 0$. These correspond to

1. **Co-rotational resonance:** $\Omega(R) = \omega$,

2. **Lindblad resonance:** $m(\Omega(R) - \omega) = \pm\kappa(R)$.

In the case that the planet is the perturbation source, $\omega = \Omega_p$, where Ω_p is the angular velocity of the planet. This means that the co-rotational resonance happens at the same R as the planet. For the Lindblad resonance, if the disk is Keplerian, $\Omega(R) = \kappa(R)$, and

$$\Omega_p = \Omega(R)\left(1 \mp \frac{1}{m}\right). \tag{3.11}$$

If the planet is in a circular orbit with semi-major axis a_p,

$$a_p^{-3/2} = R_L^{-3/2}\left(1 \mp \frac{1}{m}\right), \tag{3.12}$$

$$R_L = \left(1 \mp \frac{1}{m}\right)^{2/3} a_p, \tag{3.13}$$

where R_L is the position that Lindblad resonance takes place. This shows that Lindblad resonance can take place at multiple places. Further detailed calculation of the torques can be found in Goldreich & Tremaine (1979).

The modelling described above provides a unified framework for two different types of the migrations, namely the Type I and Type II migrations. We will review each of them in the following subsections.

3.2 Type I migration

The Type I migration happens when the planet mass is low so that the the disk structure can be approximately assumed to be unperturbed due to relatively weak planet-disk interaction. In this case the viscous torques dominates the local angular momentum transport around the planet, we can neglect the change of structure of the disk due to the planet's gravitational torques and all the resonance modes are available. The total torque Γ_{tot} that is experienced by the planet can be written as a summation of both the co-rotational and Lindblad torques

$$\begin{aligned}\Gamma_{tot} &= \sum \left(\Gamma_{L,out} + \Gamma_C\right) \\ &= \sum_{m=1}^{\infty} \Gamma_{L,out} + \sum_{m=2}^{\infty} \Gamma_{L,in} + \Gamma_C.\end{aligned} \tag{3.14}$$

Here $\Gamma_{L,in}$ and $\Gamma_{L,out}$ are the Lindblad partial torques at inner and outer resonances and Γ_C is the co-rotational torque.

The computation of the torque requires special mathematical expertise to solve the wave equations, and this is usually done by performing numerical integrations. The solutions given by Tanaka et al. (2002) shows that given a planet in a circular orbit located at R_p and the disk surface density profile $d\ln\Sigma/d\ln R = -s$, the Lindblad and corotational torques experienced by the planet can be approximated by:

$$\Gamma_L = -(2.34 + 0.10s)\Gamma_0, \tag{3.15}$$

$$\Gamma_C = (0.98 + 0.64s)\Gamma_0, \tag{3.16}$$

$$\Gamma_0 = \left(\frac{M_p}{M_*}\right)^2 \left(\frac{h_p}{R_p}\right)^{-2} \Sigma(R_p) R_p^4 \Omega_K^2(R_p), \tag{3.17}$$

where M_p/M_* is the planet-star mass ratio, h_p/R_p is the aspect ratio at the planet's position and Ω_K is the Keplerian angular velocity. More recent results with consideration of non-linear horseshoe drag can be found in Paardekooper et al. (2010) and will be introduced in section 5.1.4. To translate the torque to the motion of planet, we can introduce an e-fold migration

timescale, and the methodology will be described in Section 5.1.1.

3.3 Type II migration

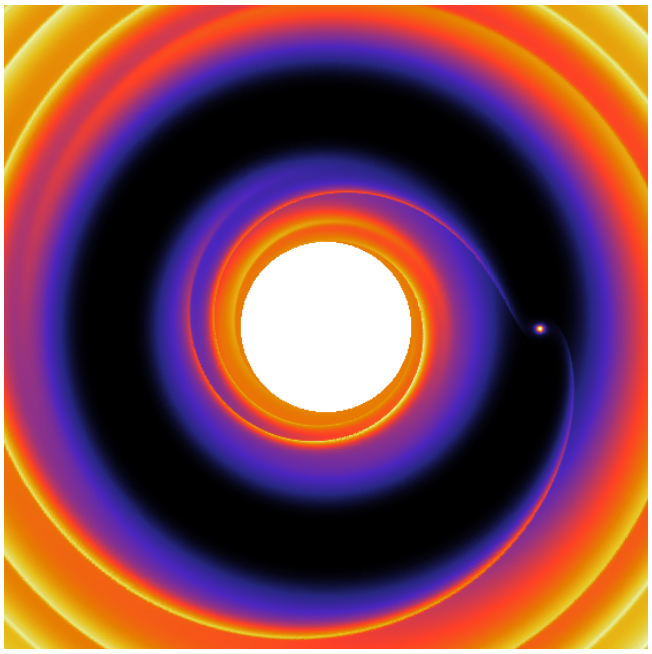

Figure 3.1: Gap carved by a giant planet, as shown by hydrodynamical simulation. Color coded according to the surface density. Credit: Dr. K. Kanagawa.

The Type II migration happens when the planet mass is high so that the viscous torques around the planet cannot compete with the strong gravitational torques exerted by the planet. As a result, the gas at the vicinity of the planet is repelled and a gap is formed since the vicious diffusion cannot replenish the gas. The low density at the gap means that all the resonant modes that are close to the planet will be ineffective, and therefore the total inward migration torque is weaker compared to that of the Type I migration. In the classical picture of Type II migration, the planet keep removing the the angular momentum of the gas from the inner edge of the gap and adding the same amount of momentum to the outer edge, and thus the inward mass flow and angular momentum flow will be unaffected as an unperturbed case without a planet. The planet will migrate inward at the same viscous speed as the gas, which we have already derived in Section 2.2.1, the equation (2.40):

$$v_R = -\frac{3\nu}{2R}. \tag{3.18}$$

Compared with Type I migration, Type II migration is much slower, which corresponds to a longer migration timescale. Following the same idea, we may think the time-scale to form a steady gap t_{gap} is equal to the viscous diffusion time derived in equation (2.47):

$$t_{gap} = \frac{h^2}{\nu}. \tag{3.19}$$

Recent studies also revealed that the depth of the gap depends on the mass, the temperature

profile and the viscosity of the disk. We will consider the dependence of these parameters in details in Chapter 5.

Chapter 4

The HL Tau system

In the previous chapters, we have already reviewed the basic properties of PPD and also interactions inside the disk, which can then be implemented numerically to perform the simulation. We are now one-step away from a complete picture of the simulation, and the last piece is the initial conditions. One of the highlights of this project is that we start from the realistic initial conditions that are deduced from the HL Tau system, a young star hosting a PPD in the Taurus star forming region. Being regarded as "an excellent example of a system just emerging from its protostellar cocoon" by Partnership et al. (2015), the HL Tau system is the first PPD observed to have the concentric ring and gap structure. Thanks to the high resolution imaging of ALMA, we are able to deduce and extract rich information from its disk structure and properties, such as the surface density profile, the gap structure and possible locations of the planets. In this chapter, we will review the observation of ALMA, the follow-up analysis and the pioneering work that links such observation to the evolution of multi-planetary system.

4.1 Disk Structure and Properties

ALMA observed the HL Tau from October 2014 to November 2014. The dust continuum images were taken at three different bands, the Band 6(1.3 mm), Band 7(0.87 mm) and Band 3(2.9 mm). The achieved resolution ranged between $0.075''$ to $0.025''$, corresponding to 10 au to 3.5 au. One can refer to Partnership et al. (2015) for the full technical details of the observation and data calibration. Figure 4.1 is the dust continuum image of HL Tau taken at Band 6(233 GHz).

Kwon et al. (2015) used both the viscous accretion and power-law disk model to fit the continuum data, and found out that the accretion model can fit better. Assuming the gas-to-dust ratio to be 100, the fitting result shows that the disk of HL Tau has a mass of $0.105(1)\,\mathrm{M}_\odot$, with inner edge at 8.78(19) au and outer edge(exponential cut-off) extended to 80.20(34) au. If the gas-to-dust ratio is assumed to be 100, the fitting result of its disk surface density can be expressed as

$$\Sigma_g(R) = 5.66 \times 10^{-4} \left(\frac{R}{80\,\mathrm{au}}\right)^{0.2} \exp\left[-\left(\frac{R}{80\,\mathrm{au}}\right)^{2.2}\right] \mathrm{M}_\odot \mathrm{au}^{-2}, \tag{4.1}$$

where R is the cylindrical distance.

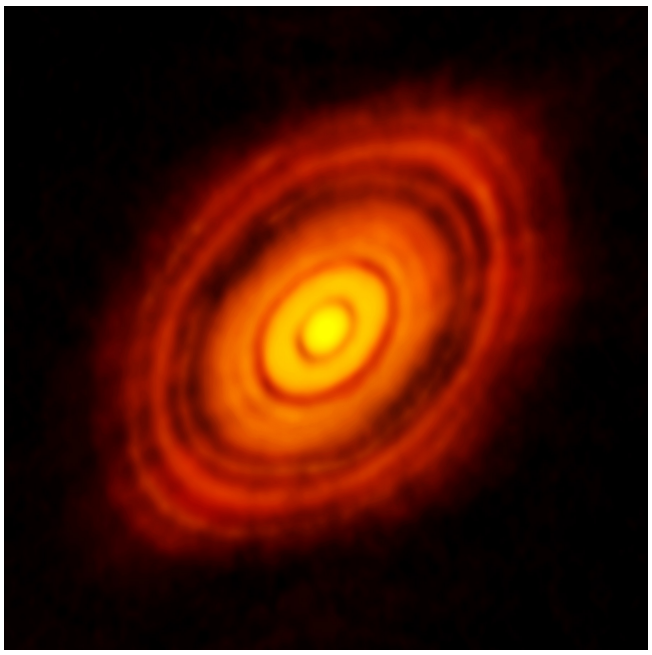

Figure 4.1: The ALMA image of HL Tau (https://www.eso.org/public/images/eso1436a/).

The accretion rate of the HL Tau is estimated to be $8.7 \times 10^{-8}\,\mathrm{M_\odot yr^{-1}}$. The upper limit of viscosity α can thus be estimated via accretion rate as

$$\alpha(R) = \frac{\dot{M}}{3\pi c_s(R) h(R) \Sigma_g(R)}. \tag{4.2}$$

At $R = 100\,\mathrm{au}$, $h \sim 10\,\mathrm{au}$, $\Sigma_g \sim 10^{-5}\,\mathrm{M_\odot au^{-2}}$. This gives the upper limit of the viscosity to be 10^{-2}. Alternatively, viscosity can also be estimated from the dust settling, and the result is in order of 10^{-4}(Pinte et al., 2015).

4.2 Planetary signatures: the gap structure

The most important accomplishment of Partnership et al. (2015) is the alternate bright and dark ring-like structure that can be clearly seen from Figure 4.1. In total seven rings and seven gaps were observed, and their respective positions and properties are summarised in Table 4.1. To avoid any confusion, we will follow the nomenclature that uses the term 'ring' to denote bright ring and 'gap' to denote the dark ring.

The discovery of the gaps deserves particular attention as it can potentially indicate the presence of giant planets. Although theories (e.g., Lin & Papaloizou, 1979; Goldreich & Tremaine, 1980; Crida et al., 2006) have long predicted that a giant planet inside a disk can gravitationally interact with its surroundings and create a gap by clearing its orbit, until Partnership et al. (2015) there was no direct proof to confirm the existence of such structures. On the other hand, alternative interpretations of the gap origin, including instability (e.g., Takahashi & Inutsuka, 2016) and snow lines (e.g., Zhang & Jin, 2015), are also possible. In this thesis, we take the assumption that the gaps are created by planets.

Recent studies on the gaps of the PPD suggested that the depth of the gap can be related the

Ring Number	Position/au	Dust Density (cm^2g^{-1})
1	20.4 ± 0.1	5.7
2	38.1 ± 0.1	6.6
3	~ 47	6.9
4	~ 55	6.8
5	68.8 ± 0.1	7.1
6	81.3 ± 0.1	4.6
7	~ 97	4.9

(a) Ring positions and dust opacity of HL Tau. Dust opacity corresponds to $\lambda = 1\,\mathrm{mm}$.

Gap Number	Position/au	Depth	Width/au
1	13.2 ± 0.2	18	12
2	32.3 ± 0.1	16	11
3	~ 42	6.9	6.6
4	~ 50	3.8	4.5
5	64.2 ± 0.1	8.0	12
6	73.7 ± 0.1	12	8.1
7	~ 91	11	9.9

(b) Gap positions and gap depth of HL Tau. Gap depth is the ratio of density at vicinity of the gap to the minimum density at the gap.

Table 4.1: Ring and gap properties of HL Tau (Partnership et al., 2015).

planet's mass, the viscosity and the aspect ratio of the disk. The analytical estimates given by Kanagawa et al. (2015) show that this relation has the form

$$\frac{\Sigma_{min}}{\Sigma} = \frac{1}{1 + 0.04K}. \tag{4.3}$$

Here Σ_{min} is the minimum density at the bottom of the gap and Σ is the density at vicinity of the gap. The dimensionless parameter K is expressed as

$$K = \left(\frac{M_p}{M_*}\right)^2 \left(\frac{h_p}{R_p}\right)^{-5} \alpha^{-1}. \tag{4.4}$$

Using two-dimensional hydrodynamical simulations, Kanagawa et al. (2016) further obtained an empirical formula which gave the relation between the width of the gap Δ_g the planet's location R_p

$$\frac{\Delta_g}{R_p} = 0.41 \left(\frac{M_p}{M_*}\right)^{1/2} \left(\frac{h_p}{R_p}\right)^{-3/4} \alpha^{-1/4}, \tag{4.5}$$

which yields the mass of the planet in terms of the gap width, aspect ratio and viscosity as

$$\frac{M_p}{M_*} = 2.1 \times 10^{-3} \left(\frac{\Delta_g}{R_p}\right)^2 \left(\frac{h_p/R_p}{0.05}\right)^{3/2} \left(\frac{\alpha}{10^{-3}}\right)^{1/2}. \tag{4.6}$$

The above equation can be used to estimate the mass of hidden planets in HL Tau. Given $\alpha = 3 \times 10^{-4}$ and the width of the respective gap, the fiducial values for the mass of the innermost three planets are estimated as 0.77, 0.11, and $0.27\,\mathrm{M_J}$ when the mass of HL Tau is $1\,\mathrm{M}\odot$.

No. of Planets	Case	a_1(au)	a_2(au)	a_3(au)	a_4(au)	a_5(au)	e_{in}	e_{out}	inc	f
5	Nominal	13.2	32.3	64.2	73.7	91.0	0	0	$[0°, 1°]$	Random
5	Resonant	13.2	32.3	64.4	74.8	90.8	10^{-5}	10^{-3}	10^{-2}	Resonant
4	Nominal	13.2	32.3	69.0	91.0		0	0	$[0°, 1°]$	Random
4	Resonant	13.2	32.3	69.1	90.8		10^{-5}	10^{-3}	10^{-2}	Resonant

Table 4.2: HL Tau initial conditions used by Simbulan et al. (2017).

4.3 Previous Study: Planetary Dynamics in HL Tau System

We have seen that a large amount of information about the possible configuration of a young multi-planetary system is hidden inside the revolutionary ALMA image of HL Tau. Simbulan et al. (2017) took this idea and connected the HL Tau image to the initial conditions of planetary systems. In this pioneering work, they extracted the orbital information from the gaps of HL Tau and systematically examined the possible outcomes of its evolution using numerical simulations. The main focus of their research is to investigate whether the initial conditions extracted from the HL Tau can reproduce a diverse configurations of multi-planetary systems that have been observed, given the allowed ranges of free parameters.

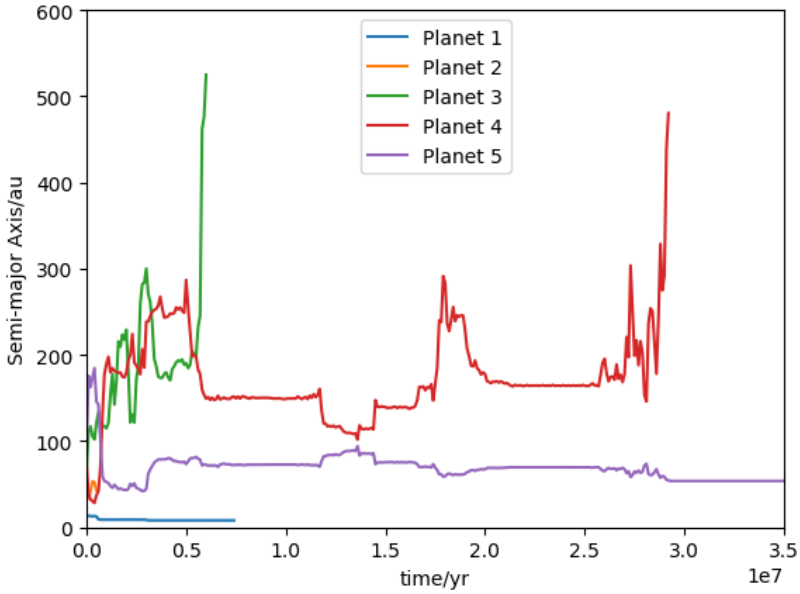

Figure 4.2: An example evolution of a 5-planet system reproduced from the initial conditions specified by Simbulan et al. (2017). The planet will be removed if it is ejected from the system or collide with the hosting star/another planet. In this system, four planets are either ejected or collided with the star within 3.5×10^7 yr, and only one planet remains.

The orbital initial conditions that were used by Simbulan et al. (2017) are summarised in Table 4.2. Since the total number of planets that HL Tau may host are unknown, they considered both the 4-planet and 5-planet cases. Each case was further divided into nominal and resonant cases: for nominal cases, the initial positions of the planets are basically assigned to be the

location of the ring; for resonant cases, the planetary systems are first allowed to enter the resonant states via a 'warm-up' test, and the real simulations will start after the resonance is reached. The mass of the planets are assumed to be equal: $1.1\,M_J$ was set to be the mass of each planet for the five-planet case and $4.7\,M_J$ for the four-planet case. Particularly, the planet mass for the four-planet case is larger than that of five-planet case since the planetary system is intentionally set to be dynamically unstable.

For each case, 100 instances with randomised phase angles were simulated and each instance was evolved up to 5 Gyr. Simulation results show that a significant fraction of planets were ejected for both five-planet and four-planet case, with some planets collided with the star or another planet. Figure 4.2 shows an example evolution of semi-major axis in a 5-planet system from initial conditions specified in Table 4.2. The surviving planets showed a diverse distribution of eccentricity, inclination and semi-major axis. Simbulan et al. (2017) also compared the results with the population of eccentric Jupiters, hot Jupiters and free-floating planets and they concluded that starting from the HL Tau initial conditions these populations can be reproduced.

We may realise that the assumption of the mass assignment that Simbulan et al. (2017) relies on is unnatural as it is intentionally biased towards unstable systems. Their work can be further extended by including the disk-planet interaction and mass accretion process, from which we can get more realistic initial conditions. As the HL Tau system is still young, it is possible that the disk-planet interaction can strongly shape the initial conditions before the disk dispersal. Further investigation can also show how the planet-disk interaction will affect the stabilities as well as the diversity of the planetary systems after long time evolution.

Chapter 5

Methods

5.1 Theoretical framework

5.1.1 Equations of Motion

When the disk is present, in addition to the gravitational forces from the central star and other planets, the planet will experience additional forces due to the disk. Consider the forces acting on the i-th planet inside the gap of the disk, the equation of motion can be written as

$$\ddot{\mathbf{r}}_i = \mathbf{f}_{\mathrm{grav},i} + \mathbf{f}_{\mathrm{a},i} + \mathbf{f}_{\mathrm{e},i} \tag{5.1}$$

where $\mathbf{r}_i$ is the position vector of the i-th planet. The $\mathbf{f}$ notations on the right hand side of the equation are respective forces *per unit mass* exerting on the *ith* planet. We assume the planets to be co-planar in this research, and thus $\mathbf{r}_i$ can be replaced by the position vector $\mathbf{R}_i$ in cylindrical coordinate system. We will continue using capital $\mathbf{R}$ to denote the cylindrical position vector unless stated otherwise.

Gravity

The first term $\mathbf{f}_{\mathrm{grav}}$ is the gravitational force exerted by the central star and other planets, which takes the form(e.g.Murray & Dermott (2000)):

$$\mathbf{f}_{\mathrm{grav},i} = -\mathcal{G}(M_* + M_i)\frac{\mathbf{R}_i}{R_i^3} + \sum_k^{k\neq i} \frac{\mathcal{G}M_k}{\parallel \mathbf{R}_k - \mathbf{R}_i \parallel^3}(\mathbf{R}_k - \mathbf{R}_i) - \sum_k^{k\neq i} \frac{\mathcal{G}M_k}{R_k^3}\mathbf{R}_k, \tag{5.2}$$

where $R = |\mathbf{R}|$. As in the previous chapters, we use symbol $*$ to denote the central star and subscripts i, k as the indices of planets *only*. Since later we are going to perform the N-body simulation framework to carry out the simulations, in practice this term requires no special attention as it has been fully absorbed into the N-body integration framework.

Migration force

The second term $\mathbf{f}_{a,i}$ denotes the force that drives the inwards-migration of planets. As discussed in Section 3, a planet with index i embedded inside the disk experiences an effective torque Γ_i and migrates inwards. We define an e-fold migration timescale $\tau_{a,i}$

$$\frac{\dot{a}_i}{a_i} \equiv -\frac{1}{\tau_{a,i}}, \tag{5.3}$$

where a_i is the semi-major axis of the planet. To see the physical meaning of $\tau_{a,i}$, assuming small eccentricity, we can write the migration velocity $\dot{\mathbf{R}}_i$ in terms of the torque and angular momentum as:

$$\dot{\mathbf{R}}_i = \frac{2\Gamma_i}{L_i}\mathbf{R}_i, \tag{5.4}$$

where $L_i = a_i^2 \Omega_{K,i} M_i$ is the orbital angular momentum, $\Omega_{K,i}$ is the Keplerian angular velocity at R_i. For small eccentricity, $|\mathbf{R}_i| \approx a_i$, and equation (5.4) implies

$$\tau_{a,i} = -\frac{L_i}{2\Gamma_i}. \tag{5.5}$$

To incorporate this migration into the N-body simulation, we implement the migration as an effective force. Further differentiation of equation (5.4) gives the acceleration:

$$\ddot{\mathbf{R}}_i = \frac{\Gamma_i \dot{\mathbf{R}}_i}{M_i a_i^2 \Omega_{K,i}} = \frac{\Gamma_i}{L_i}\dot{\mathbf{R}}_i. \tag{5.6}$$

Substituting equation (5.5) to (5.6) then the expression of $\mathbf{f}_{a,i}$ is simply

$$\mathbf{f}_{\mathrm{a},i} = \ddot{\mathbf{R}}_i = -\frac{\dot{\mathbf{R}}_i}{2\tau_{a,i}}. \tag{5.7}$$

Eccentricity damping force

The disk also tends to circularise the planet's orbit if the planet is in a eccentric orbit. Using the same spirit as equation 5.3, we define the eccentricity damping timescale, $\tau_{e,i}$ and assume the following linear relationship with $\tau_{a,i}$(Lee & Peale, 2002; Kley et al., 2004):

$$\tau_{e,i} = \tau_{a,i}\left(\frac{h_i}{R_i}\right)^2 c, \tag{5.8}$$

where h/R is the aspect ratio and c is a constant. Following Kanagawa et al. (2018), we take $c = 1.282$ in our simulation. We can then compute the eccentricity damping force as

$$\mathbf{f}_{\mathrm{e},i} = -\frac{\mathbf{v}_i}{(1-e_i^2)(3/2)\tau_{e,i}} + \hat{\mathbf{l}}_i \times \hat{\mathbf{R}}_i \sqrt{\frac{\mu}{a_i(1-e_i^2)}} \frac{1}{(3/2)\tau_{e,i}}, \tag{5.9}$$

where $\mathbf{v}_i = \dot{\mathbf{R}}_i$ and $\hat{\mathbf{l}}_i$ is the unit vector of the specific angular momentum.

5.1.2 Model of the Disk Structure Hosting Multiple Planets

In sections 2.2.1 and 2.2.2, we reviewed the classical picture of the disk surface density profile and derived the static solution. Since our simulations takes account of the change of surface density due to mass accretion onto the planets, we generalised equation (2.53) to the N-planet case to make it applicable in multi-planetary systems.

Consider the steady state with in total N planets located at R_i, $i \in \{1, 2, ..., N\}$, and treat each planet as a mass sink with accretion rate $\dot{M}_i$. Then the conservation of mass gives

$$\dot{M}(R) = \begin{cases} \dot{M}_* & (R < R_1), \\ \dot{M}_* + \sum_{i=1}^{n} \dot{M}_i & (R_n < R < R_{n+1}, n \in \{1, 2, ...N-1\}), \\ \dot{M}_* + \sum_{i=1}^{N} \dot{M}_i & (R > R_N). \end{cases} \tag{5.10}$$

Similarly, conservation of the angular momentum flow gives

$$\dot{M}(R)j(R) = \begin{cases} \dot{M}_* j_* & (R < R_1), \\ \dot{M}_* j_* + \sum_{i=1}^{n} \dot{M}_i j_i & (R_n < R < R_{n+1}, n \in \{1, 2, ...N-1\}), \\ \dot{M}_* j_* + \sum_{i=1}^{N} \dot{M}_i j_i & (R > R_N), \end{cases} \tag{5.11}$$

where $j_i = j(R_i) = R_i^2 \Omega_i$ is the specific angular momentum. Now consider the case of when $R_n < R < R_{n+1}$. Using the boundary conditions at $R = R_i$, we can solve equation (2.49) as

$$3\pi\nu j(R)\Sigma_g(R) = \dot{M} j(r) - \dot{M}_* j_* - \sum_{i}^{n} \dot{M}_i j_i. \tag{5.12}$$

Substituting equation 5.10 to the above equation, we have

$$\begin{aligned} \Sigma_g(R) &= \frac{\dot{M}_*}{3\pi\nu}\left(1 - \frac{j_*}{j(R)}\right) + \sum_{i=1}^{n} \frac{\dot{M}_i}{3\pi\nu}\left(1 - \frac{j_i}{j(R)}\right) \\ &= \frac{\dot{M}_*}{3\pi\nu}\left(1 - \sqrt{\frac{R_*}{R}}\right) + \sum_{i=1}^{n} \frac{\dot{M}_i}{3\pi\nu}\left(1 - \sqrt{\frac{R_i}{R}}\right). \end{aligned} \tag{5.13}$$

The above formula shows that given the positions of all the planets, the surface density at position R is specified by the accretion rate $\dot{M}_i$ alone. We define the global accretion rate as the sum of all the accretion rates:

$$\dot{M}_{glob} = \dot{M}_* + \sum_{i=1}^{N} \dot{M}_i \tag{5.14}$$

Our simulation assumes that $\dot{M}_{glob}$ is a constant. It can be seen from the next section that once $\dot{M}_{glob}$ and the planet system configuration are specified, the individual $\dot{M}_i$ can be calculated iteratively.

We adopt a simple exponential decaying model to account for the time dependence of the surface density due to disk dispersion:

$$\Sigma_g(R,t) = \Sigma_g(R) \exp\left(-\frac{t}{\tau_{disk}}\right), \tag{5.15}$$

where τ_{disk} is the e-fold disk lifetime. Since the disk lifetime is very uncertain, we treat τ_{disk} as a global free parameter in the simulation and consider different values.

5.1.3 Accretion Model

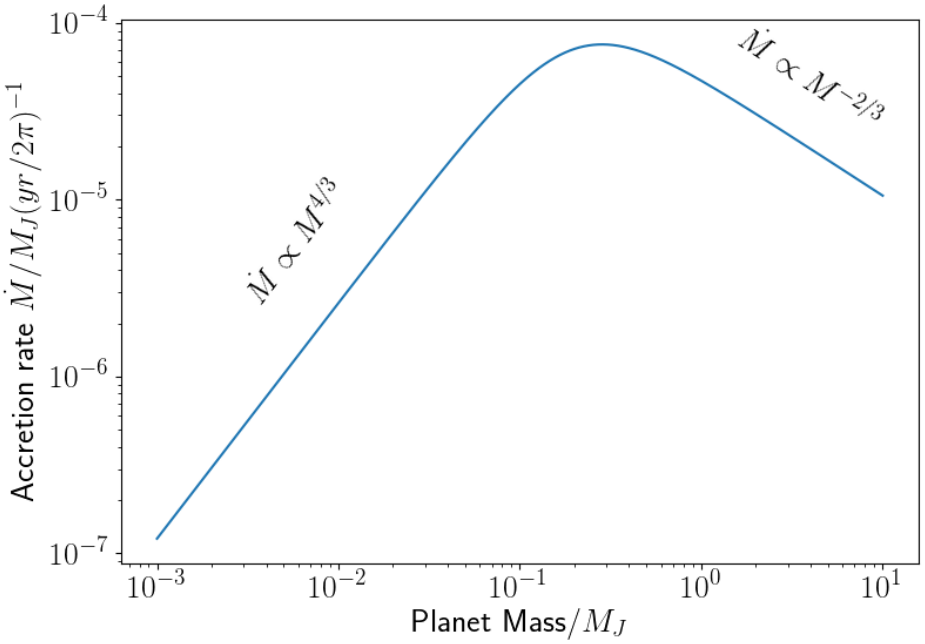

Figure 5.1: The planetary accretion rate against the planet mass(single planet) at constant $\Sigma_{R=5\,\mathrm{au}}$. Parameters: $\alpha = 4 \times 10^{-3}$, $R_p = 5.2\,\mathrm{au}$, $M_* = 1\,\mathrm{M}_\odot$, $\dot{M}_* = (2\pi)^{-1}10^{-8}\,\mathrm{M}_\odot\mathrm{yr}^{-1}$.

We follow Tanigawa & Tanaka (2016) to determine the accretion rate of each planet, $\dot{M}_i$. This model shows the accretion rate is related to the accretion surface density(disk surface density at the planet's accretion site) Σ_{acc} as

$$\dot{M}_i = D_i \Sigma_{acc,i}, \tag{5.16}$$

where D_i is the accretion area of the protoplanetary disk per unit time given by

$$D_i = 0.29 \left(\frac{h_i}{R_i}\right)^{-2} \left(\frac{M_i}{M_*}\right)^{4/3} R_i^2 \Omega_i. \tag{5.17}$$

In the above, Ω_i is the angular velocity of the i-th planet, which may not be equal to $\Omega_{K,i}$; nevertheless we take the approximation that $\Omega_i \approx \Omega_{K,i}$. We also assume that the accretion density is roughly equal to the minimum density at the bottom of the gap, which can be

expressed as(c.f. equation 4.3)

$$\Sigma_{acc,i} \approx \Sigma_{min,i} = \frac{1}{1 + 0.034K_i}\Sigma(R_i), \tag{5.18}$$

where $\Sigma(R_i)$ is given by equation (5.13) and K is a dimensionless factor related to the depth of the gap(equation (4.4)):

$$K_i = \left(\frac{M_i}{M_*}\right)^2 \left(\frac{h_i}{R_i}\right)^{-5} \alpha^{-1} \tag{5.19}$$

Figure 5.1 shows how the accretion rate varies with the planet mass given the parameters specified. The accretion rate first increases as mass increases from $M_i = 10^{-3}\,\mathrm{M_J}$, reaches maximum when the planet mass is around $3 \times 10^{-1}\,\mathrm{M_J}$, and then decreases as mass increases further. From equation (5.18), when the planet mass is small so that $K_i \ll (0.034)^{-1}$, $\dot{M}_i \propto D \propto M_i^{4/3}$; When the planet mass get larger and $K_i \gg (0.034)^{-1}$, K_i dominates the denominator and thus $\dot{M}_i \propto D \propto M_i^{(-2/3)}$.

5.1.4 Migration Model

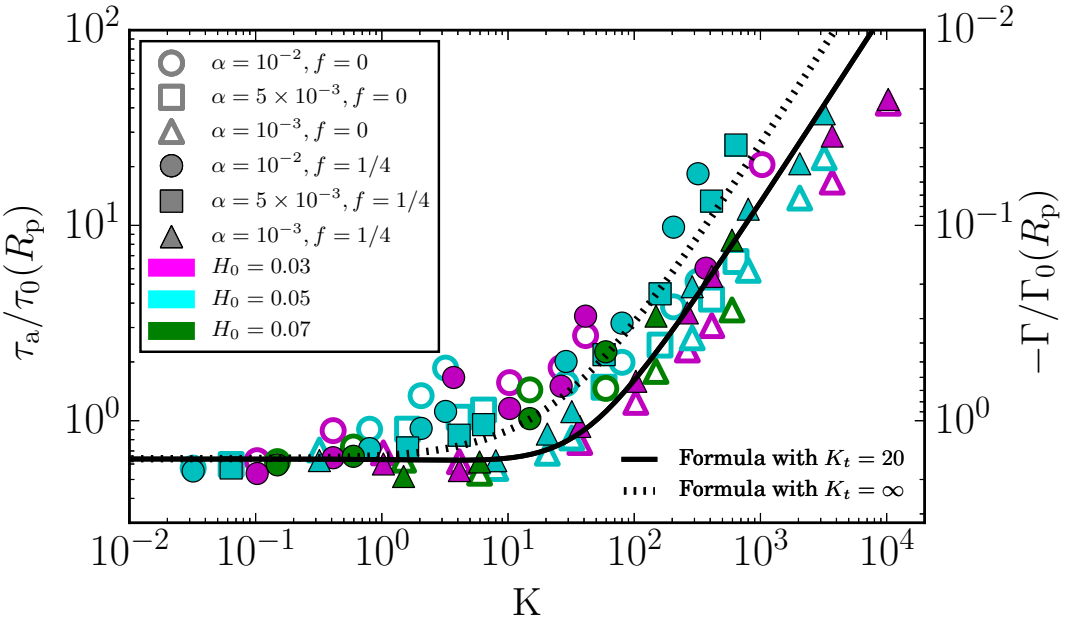

Figure 5.2: The dimensionless migration time-scale versus the K value. Coloured symbols represent results of the hydrodynamical simulations, which shows good agreement with the model prediction (Kanagawa et al., 2018).

In Section 5.1.1 we defined the migration time-scale $\tau_{a,i}$ to empirically capture the physics of the migration process. Here we adopted τ_a expression from Kanagawa et al. (2018), as shown by Figure 5.2. Their model connects both Type I and Type II migration of the planets in a

single framework. In this model, the migration time-scale of the i-th planet $\tau_{a,i}$ is expressed as

$$\tau_{a,i} = \frac{1 + 0.04K_i}{\gamma_{L,i} + \gamma_{C,i}\exp(-K_i/K_t)}\tau_{0,i}(R_i), \tag{5.20}$$

where $\gamma_{C,i}$ and $\gamma_{L,i}$ are the ratios between the torques $\Gamma_{C,i}$ and $\Gamma_{L,i}$ to the characteristic torque $\Gamma_{0,i}$, respectively, K_t is the co-rotational cut-off value of K_i. The characteristic time-scale $\tau_{0,i}$ is defined as

$$\tau_{0,i} = \frac{L_i}{2\Gamma_{0,i}}. \tag{5.21}$$

The explicit expressions of γ are adopted from Paardekooper et al. (2010) assuming locally isothermal disk:

$$\gamma_{C,i} = \frac{\Gamma_{c,i}}{\Gamma_{0,i}(R_i)} = 1.1(1.5 - s)b_i + 2.2\beta b_i^{0.71} - 1.4\beta b_i^{1.26}, \tag{5.22}$$

$$\gamma_{L,i} = \frac{\Gamma_{L,i}}{\Gamma_{0,i}(R_i)} = -(2.5 - 0.1s + 1.7\beta)b_i^{0.71}, \tag{5.23}$$

where $b_i = (0.4h_i)/\epsilon$, ϵ is the softening parameter, $s = -d\ln\Sigma/d\ln R$ is the surface density gradient, $\beta = -\ln T/\ln R$ is the temperature gradient, and $\Gamma_{0,i}$ is defined as

$$\Gamma_{0,i}(R_i) = \left(\frac{M_i}{M_*}\right)^2 \left(\frac{h_i}{R_i}\right)^{-2} \Sigma(R_i)R_i^4\Omega_{K,i}^2. \tag{5.24}$$

We may notice that K value controls the evolution of the migration. When the planet mass is small, small K value indicates the gap is not formed, and thus the migration is dominant by Type I migration and the time-scale is short. As the planet gains enough mass from accretion, K gradually increases, indicating that a gap is formed and the slower Type II migration becomes dominant, resulting in larger migration time-scale. The dependence on K also shows the strong coupling between the mass accretion and the migration of the planet.

5.2 Numerical Approaches

Since the strong coupling among the surface density evolution, planetary migration and accretion of the planet is difficult to consider analytically, we resorted to numerical integration, namely the modified N-body simulations. Based on the original N-body gravitational simulation, we implemented the planet-disk interactions as additional forces and then incorporated into the N-body framework.

5.2.1 Simulation Environment

Our simulation uses the publicly available N-body code `REBOUND`(Rein & Liu, 2011) and its extension `REBOUNDx`. Both `REBOUND` and `REBOUNDx` are also used by Simbulan et al. (2017). Since they are originally developed for generic-purpose gravitational N-body simulation, there are a variety of choices to customise `REBOUND` and tailor it to our purpose. Among the integrators that

are available in REBOUND, we choose the ias15 integrator(Rein & Spiegel, 2014), which is a non-symplectic, adaptive time-step integrator down to machine precision(10^{-15}) over 10^9 dynamical time-scales. Before the actual simulation, We systematically went through various tests to ensure the reliability of this integrator, and the test results will be presented in Appendix A.

REBOUNDx is an extension to REBOUND developed by D.Tamayo, who is one of the major contributors to the REBOUND as well. Although REBOUND itself has an option to specify customised force, the functionality is rather limited. REBOUNDx provides the interface to introduce additional forces and post-orbit modification, which allows implementation of a wider range of interactions and effects, such as velocity-dependent drag force and mass modification. Within the framework of REBOUNDx, we implemented the additional forces in Section 5.1.1 and mass accretion in 5.1.3 as force modules and calculated the real-time surface density using iterative methods.

We performed all the major calculations on computation clusters powered by Linux environment at Centre for Computational Astrophysics(CfCA), National Astronomical Observatory of Japan(NAOJ). We adopted gcc compilers to compile the C code, and the results were analysed by Python 3.7.

Notation	Meaning	Type	Range	Fiducial Value
Varied Parameters				
f	Flaring index	varied	$0.15 - 0.35$	0.25
$\tau_{\rm disk}$	Disk lifetime	varied	$1 - 3$Myr	2 Myr
α	Shakura's Viscosity	varied	$2 \times 10^{-4} - 6 \times 10^{-4}$	3×10^{-4}
Disk-Related				
$M_{\rm disk}$	Disk mass	fixed		$0.105 M_\odot$
$\Sigma_g/\Sigma_{\rm dust}$	Gas-to-dust ratio	fixed		100
$(h/r)_{1\,\rm au}$	Aspect Ratio at 1 au	fixed		0.03
M_*	Stellar Mass	fixed		$1.0 M_\odot$
Γ_C	Co-rotational torque			
Γ_L	Lindblad torque			
R_{in}	Disk inner edge	fixed		10 au
R_{out}	Disk outer edge	fixed		80 au
Γ_0	Characteristic torque			
γ_C	Γ_C/Γ_0			
γ_L	Γ_L/Γ_0			
K	Gap depth parameter			
K_t	Co-rotation cut-off	fixed		20
Planet-Related				
N	Number of planets	fixed		3
a_1^i, a_2^i, a_3^i	Initial semi-major axis	fixed		13.2, 32.3, 73.7au
e_1^i, e_2^i, e_3^i	Initial eccentricity	fixed		10^{-7}
i_1^i, i_2^i, i_3^i	Initial inclination	fixed		0
M_1^i	Initial Planet 1 Mass			$1.4(\alpha/10^{-3})^{1/2} M_{\rm J}$
M_2^i	Initial Planet 2 Mass			$0.2(\alpha/10^{-3})^{1/2} M_{\rm J}$
M_3^i	Initial Planet 3 Mass			$0.5(\alpha/10^{-3})^{1/2} M_{\rm J}$

Table 5.1: Initial parameters and variables in our simulation. The superscript 'i' stands for the initial value of planet-related parameters.

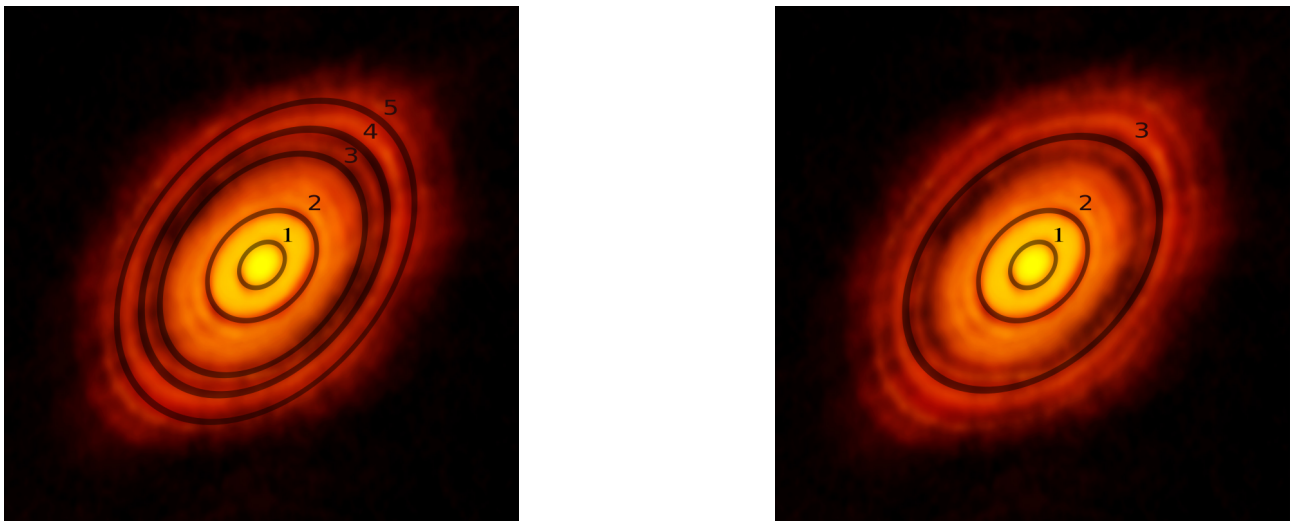

(a) 5-Planet case in Simbulan et al. (2017).

(b) 3 planets in our simulation

Figure 5.3: Comparison between the initial locations of the planets in Simbulan et al. (2017) and our simulation. The number represents the index of each planet.

5.2.2 Parameters and Initial Conditions

Table 5.1 summarises all the parameters and intermediate variables employed in the simulation. We have surveyed 5 values of the flaring indices f, 3 values of the disk lifetime τ_{disk} and 5 values of the viscosity α parameter. The surveyed values are in equal interval within the range specified in Table 5.1. We therefore simulated 75 instances for 3 planets each, and thus there are 225 planets in total.

We fix the star mass to be $1.0\,M_{\odot}$, and we set the disk mass to be $0.105\,M_{\odot}$(Kwon et al., 2015). We also fix the initial positions of the planets to be 13.2, 32.3 and 73.7 au, which corresponds to the top three deepest gap stated in Pinte et al. (2015). The initial positions of the planets are also identical to those of the first, second and fourth planets of the "5-planet-nominal" case in the investigation of Simbulan et al. (2017), shown by Figure 5.3. We assume that the planets are initially in near-circular orbits and set the initial eccentricity to be identical 10^{-7} for all three planets. All planets are set to have zero inclination and their orbital phases are randomised. The values of the initial mass are determined by the model from Kanagawa et al. (2016), which deduced the planet mass from the gap width. In this model the initial planet mass is scaled by $\alpha^{1/2}$, and since α is a free parameter that has been surveyed, we vary the initial mass of the planet according to the different α values.

5.2.3 Simulation Structure

We divide the simulation into two stages, as illustrate by Figure 5.4: the disk stage and the disk-free stage. At the disk stage, the planet-disk interaction and mass accretion modules are switched on. The total simulation time for this stage is set to be $3\tau_{disk}$. At $3\tau_{disk}$, most of the gas has already been removed, which is effectively the end of the planet-disk interaction. The orbital information of all three planets as well as other parameters are stored every $(10^3/2\pi)$yr.

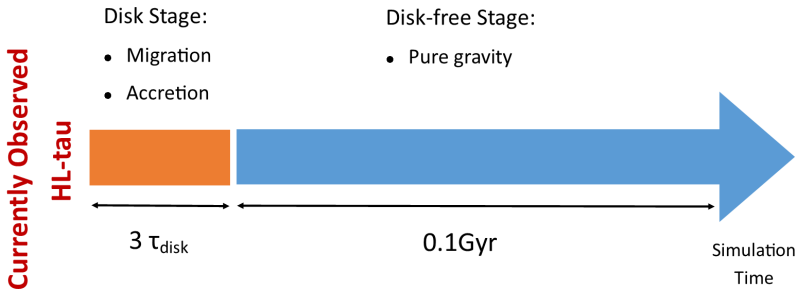

Figure 5.4: Illustration of the timeline of the two-stage simulation.

At the disk-free stage, only gravitational force is considered. The initial conditions at this stage were extracted from the final states of the previous stage and the system is evolved for another 0.1 Gyr. Ideally we should evolve the system for around 1 to 2 Gyr, which correspond to the mode of stellar age reported by Walkowicz & Basri (2013). However, due to the limited computing time of the simulation, we take 0.1 Gyr as a final epoch of the simulation. We plan to continue the simulation later, but according to the previous criteria of the instability time-scale, most of our systems are supposed to have the least instability time at around 0.1 Gyr(see section 6.2.1), therefore N-body simulation up to 0.1 Gyr is expected to be useful in understanding the final outcome of the system to some extent. The output interval at this stage is $(10^5/2\pi)$yr.

Chapter 6

Results

In the previous chapter, we described the two-stage numerical approach and the implementation of various interactions. This final chapter will be devoted to present the simulation results at $3\tau_{\rm disk}$ and 0.1 Gyr after disk dispersal, with the corresponding post-analysis of the emerging trends and patterns breaking down in different parameter spaces. We will also investigate on the stability of the systems with references to the empirical stability criteria.

6.1 Evolution during the Disk-planet Interaction ($t < 3\tau_{\rm disk}$)

6.1.1 A Typical Example of Planetary Evolution

For the disk phase, we simulated in total 75 instances of 3-planet system, with interactions implemented and initial conditions described in Section 5.2. Figures 6.1 and 6.2 show an example of their evolution. The three free parameters mentioned in Section 5.2.2 are chosen to be the best-guess fiducial values: flaring index $f = 0.25$, disk lifetime $\tau_{\rm disk} = 2\,{\rm Myr}$ and viscosity $\alpha = 3 \times 10^{-4}$. The evolution time for this case is $3\tau_{\rm disk} = 6\,{\rm Myr}$.

An example of the evolution of semi-major axis and mass is shown in Figure 6.1. Within 6 Myr, planets $1, 2, 3$ migrates from $[13.2, 32.3, 73.7]$au to $[1.97, 3.27, 5.55]$au and their masses also increase from $[0.77, 0.11, 0.27]{\rm M_J}$ to $[1.84, 2.36, 4.23]{\rm M_J}$. In the first 0.3 Myr, the outer two planets(planet 2 and 3) quickly grow and migrate inward, and until planet 2 becomes close enough to planet 1, the migration of the inner-most planet (planet 1) does not commence. As the mass of the planet grows, planets carve the gap, switch to Type II migration, and the migration speed slows down. The three planets then continue growing and migrating inward together, and gradually reach their final states as the disk density decays.

The details of the migration history can be further revealed from Figures 6.1c and 6.1d , which shows the evolution of eccentricity and migration time-scale, respectively. The eccentricity of planet 2 is firstly excited due to the encounter of planet 3; the second excitation, together with that of planet 1, happens at the same time when planet 1 encounters planet 2 and starts to migrate. Due to the eccentricity damping of the disk, the eccentricities of both planet 1 and 2

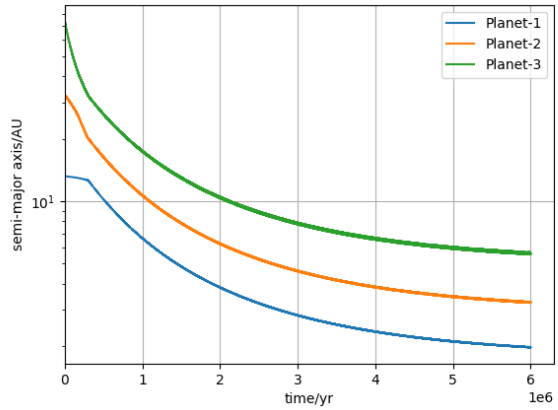

(a) Semi-major axis evolution

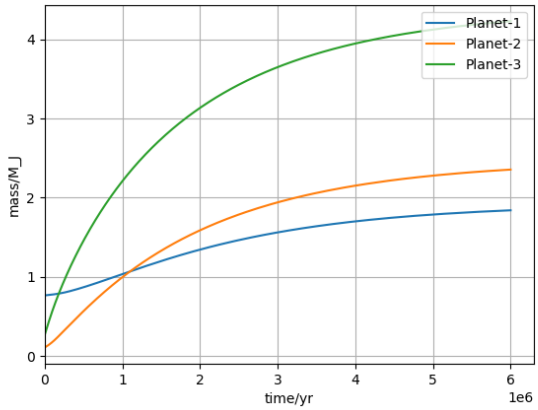

(b) Mass evolution

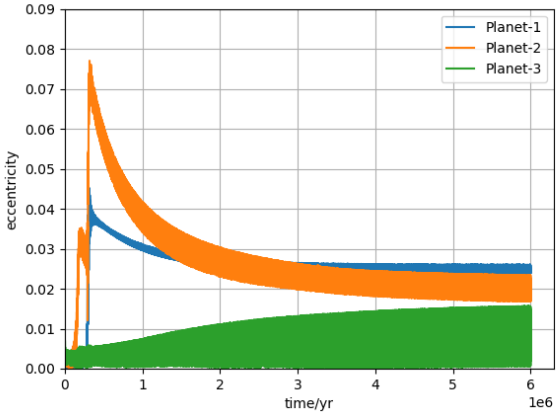

(c) Eccentricity evolution

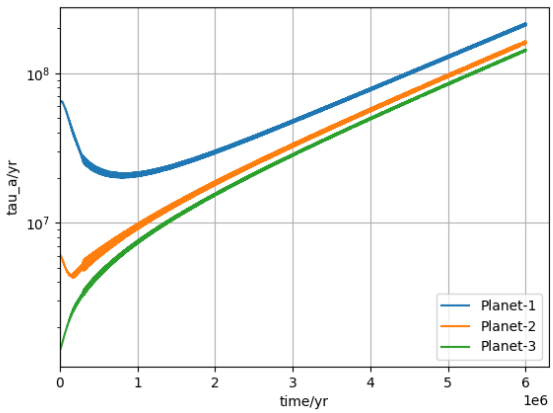

(d) Migration time scale τ_a evolution

Figure 6.1: An example of the evolution of a, m, e and τ_a for planets 1, 2 and 3 ($f = 0.25$, $\tau_{disk} = 2\,\text{Myr}$ and $\alpha = 3 \times 10^{-4}$).

are then damped along the evolution and reach the same level at the end, which is about 0.02. The migration time-scale also shows similar features. Except the planet 3, both planet 1 and 2 have experienced similar "acceleration-maximum-deceleration" dips in their migration process, as shown in Figure 6.1d. It is worth noting that once three planets start to migrate together, their migration time-scales also tend to grow at almost the same rate.

Figure 6.2 shows the evolution of the gas surface density Σ_g. Figure 6.2a shows the global surface density profile at different epochs, while Figure 6.2b shows the surface density at the locations of the planets. We neglect the detailed structure of the gaps. At $t = 0$, the strong mass accretion on the outside planets 2 and 3 creates a steep bump on the profile, and therefore both the migration and accretion of the planet 1 are quenched. The rapid inward migration of planet 2 and 3 results in increase of the surface densities at their respective positions. As the mass of planet 2 and 3 continues to grow, their accretion rates drop as $\dot{M}_i \propto M_i^{-2/3}$, causing the density bumps becomes less steep and raising the surface density at the location of planet 1. At $t = 2\,\text{Myr}$, since the planet system becomes more packed together and accretion rates of all three planets drop to low level, the bumps become almost negligible. The density at location of each planet reaches the maximum, and then drops as the global disk decaying dominates

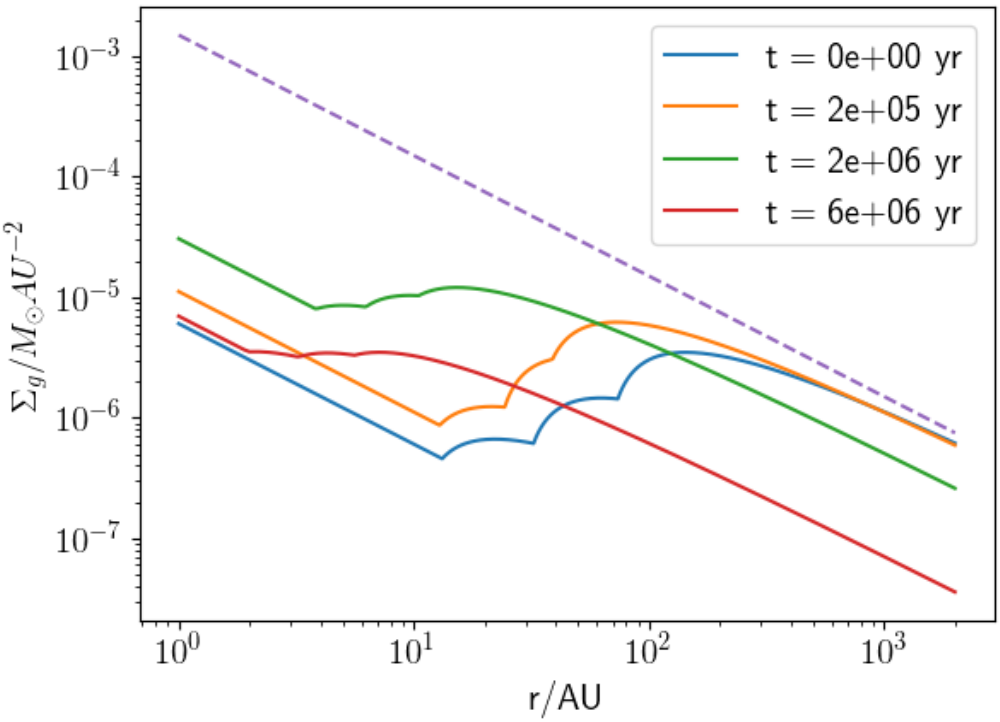

(a) The global evolution of the gas surface density profile. The purple dotted line is the unperturbed density profile at $t = 0$ if no planet is present. Planets are located at the discontinuous dips of each line.

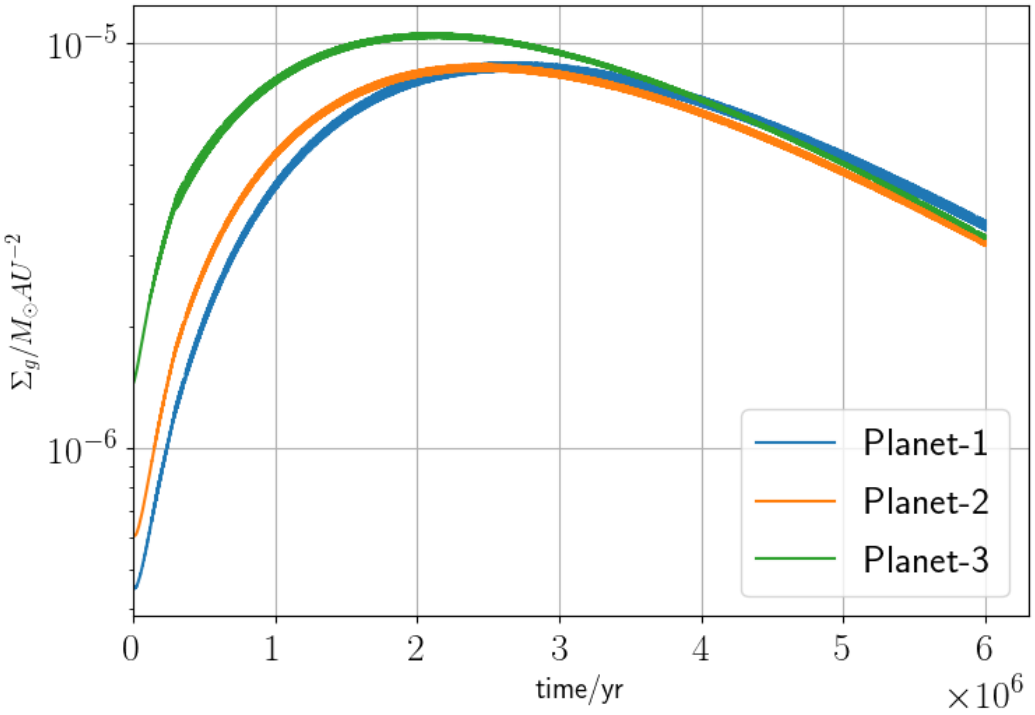

(b) Variation of the gas surface density at the planet's location R_i. Note that R_i also varies with time due to migration.

Figure 6.2: Global evolution of the gas surface density profile and the evolution of gas surface density at each planet's location.

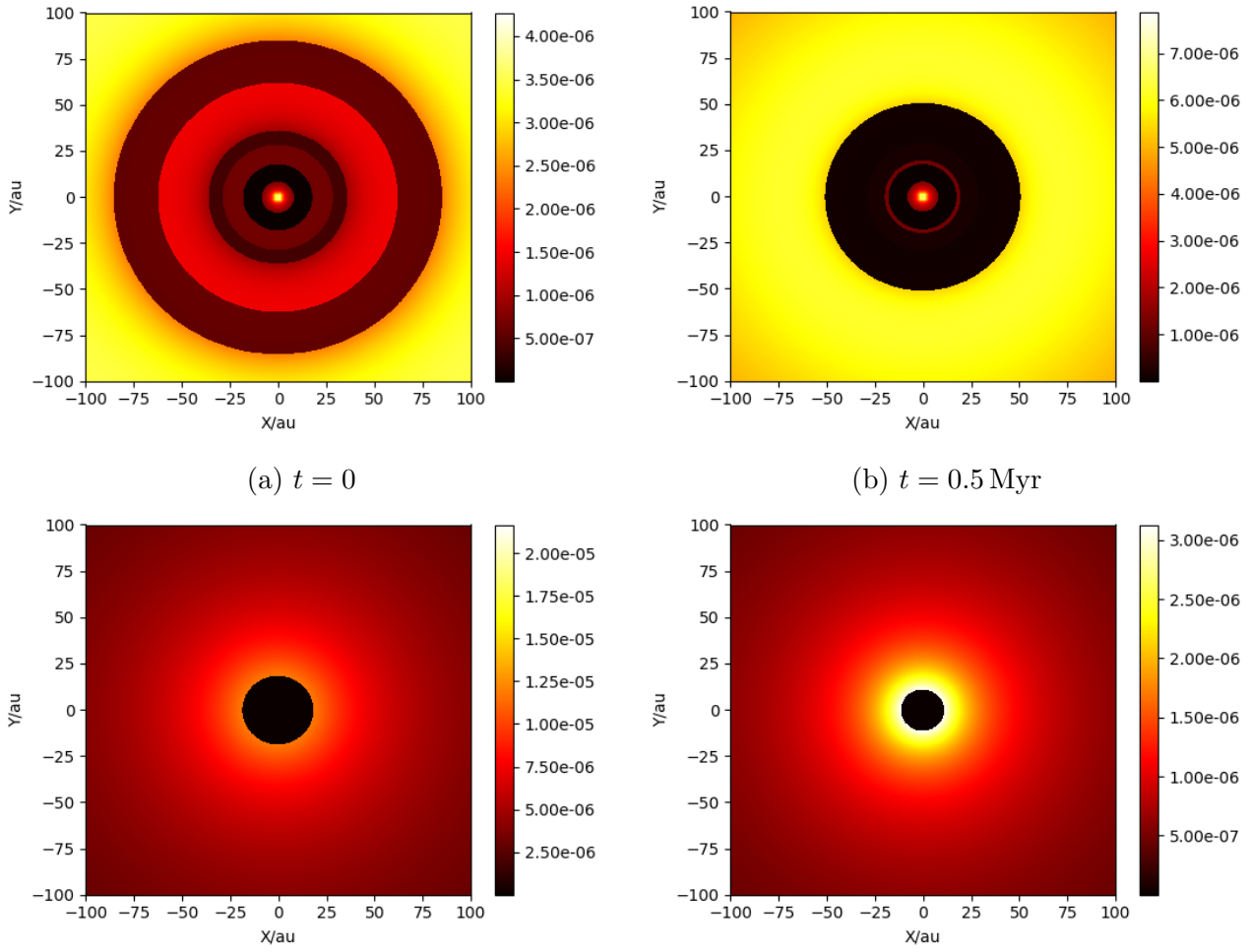

(a) $t = 0$ (b) $t = 0.5\,\mathrm{Myr}$

(c) $t = 2\,\mathrm{Myr}$ (d) $t = 6\,\mathrm{Myr}$

Figure 6.3: 2-D visualisation of the disk surface density at different epochs. The colour bar at the side represents the surface density at each epoch in units of $\mathrm{M}_{\odot}\mathrm{au}^{-2}$.

the change of surface density. The same trend continues and at $t = 6\,\mathrm{Myr}$ the density bumps become further negligible and the surface density of planet 1 starts to surpass those at planets 2 and 3, as the global profile tends to be a straight line with gradient proportional to ν^{-1}.

To visualise the evolution of the disk surface density, we also plot the gas surface density at 4 different epochs in two dimentional heat maps, shown by Figure 6.3. The width of the gap is given by equation (4.5) and the surface density inside the gap is given by equation (5.18). For illustration purposes we ignore the detailed structure of the gap and assume that the boundary of the gap is like a step function. At $t = 0$, there are three separate gaps and each centred at the initial orbit of the respective planet. At 0.5 Myr, due to the inward migration of the outermost planet, the third gap combined with the second gap. The migration continues and at 2 Myr, all three gaps merge into a single gap and an inner-hole is formed. At 6 Myr, the size of the hole shrinks as all planets migrate further inward. When the gaps are combined, the migration speed may deviate from that given by equation (5.20), since the depth and width of the common gap is different from the gap formed by a single planet(e.g., Duffell & Chiang, 2015). In the future, we need to investigate the impacts on the formation of the common gap on the migration speed and accretion rate onto the planet.

6.1.2 Distribution of Planet Mass and Semi-major axis

The overall distribution of the planets after the disk-phase is plotted in Figure 6.4, where a is the semi-major axis in units of au and m is the mass of the planet in units of $\mathrm{M_J}$. Overall we found that the final position of the planets stretched from around 0.007 au to 30 au, with the final mass ranging from 0.4 $\mathrm{M_J}$ to around 10 $\mathrm{M_J}$. The general trend shows that the closer the planet to the star, the larger the mass of the planet. Since the initial mass of the planets range from Saturn mass to one Jupiter mass and there is no mass reduction mechanism implemented, it is expected that mass of some planets can grow up to the brown dwarf mass while migrating to the very inner region given long enough disk lifetime. As mentioned in the previous chapter, we will set the final results at $3\tau_{disk}$ to be the initial conditions of the disk-free stage. On the same graph, we make the comparison between initial conditions that are used in Simbulan et al. (2017) and our results. The comparison suggests that the configuration of the planetary system can undergo dramatic changes and become more diverse after including the disk migration and accretion mechanism.

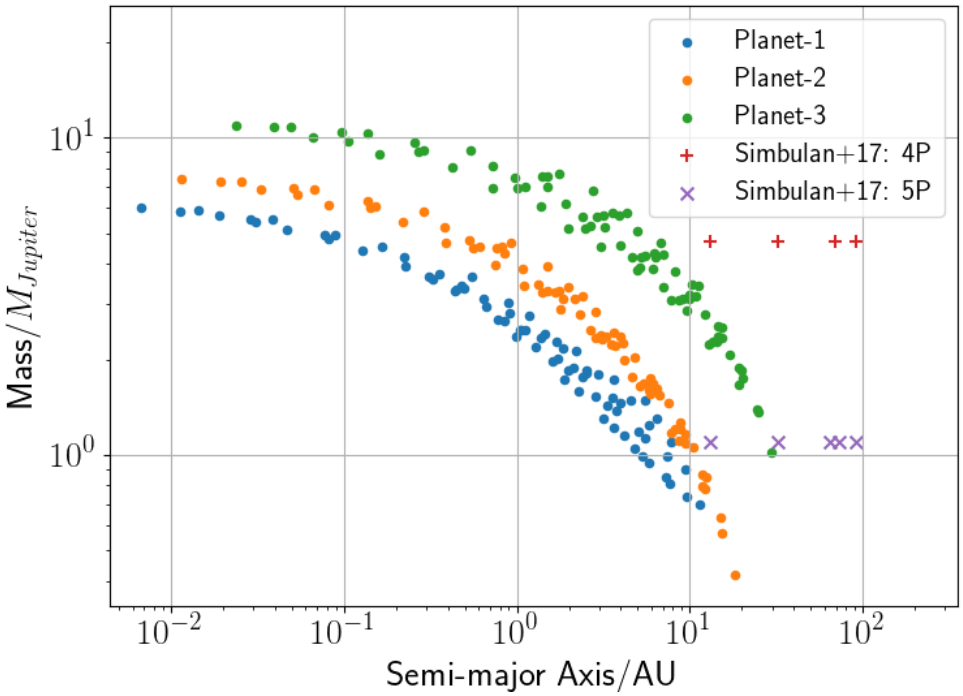

Figure 6.4: Overall Distribution of Planet's mass $m/M_{Jupiter}$ in the semi-major axis a/au after disk phase. Planet 1, 2, 3 refers to the planet initially positioned at 13 au, 32 au, 74 au. Labels 'Simbulan+17: 4P' and 'Simbulan+17: 5P' correspond to 4-planet and 5-planet cases in Simbulan et al. (2017).

6.1.3 Parameter Dependence of Planetary Mass and Semi-major Axis

The overall final distribution shown in Figure 6.4 does not reveal individual dependence of m and a on f, τ_{disk} and α. We thus break down the distribution into different parameter spaces

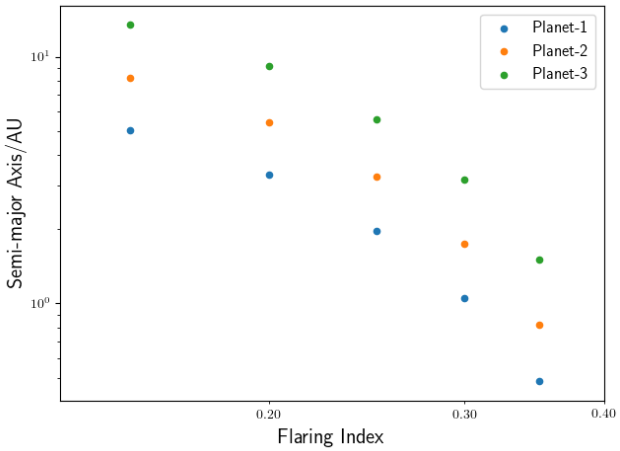

(a) Semi-major axis versus flaring index.

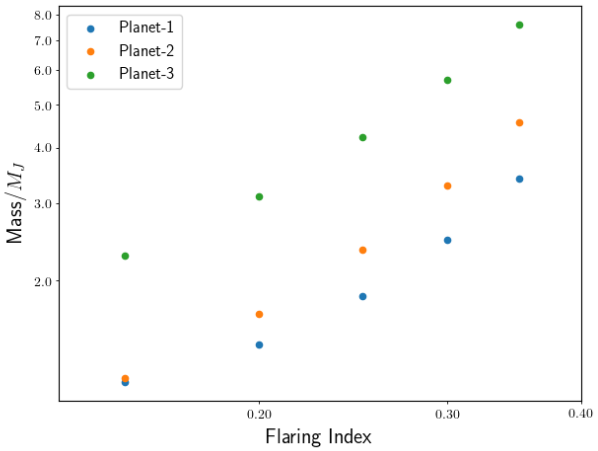

(b) Mass versus flaring index f.

Figure 6.5: Semi-major axis and Mass dependence on flaring index.

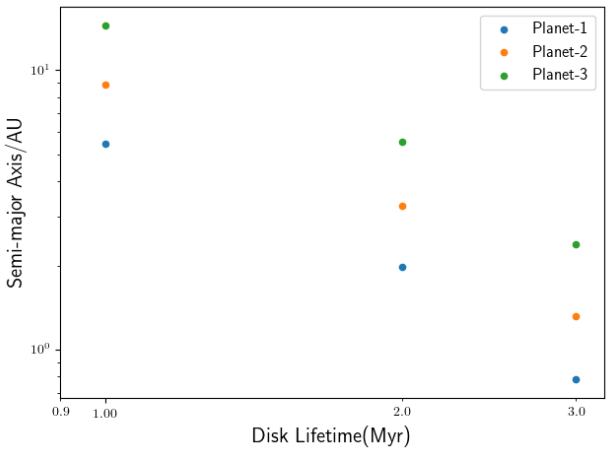

(a) Semi-major axis versus Disk lifetime τ_{disk}.

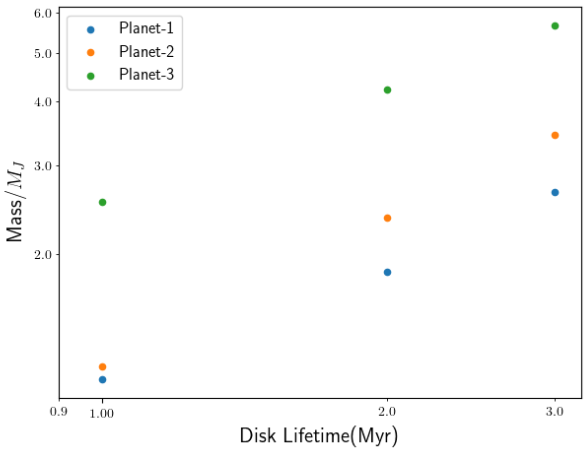

(b) Mass versus $\tau_{\rm disk}$.

Figure 6.6: Semi-major axis and Mass dependence on disk lifetime $\tau_{\rm disk}$.

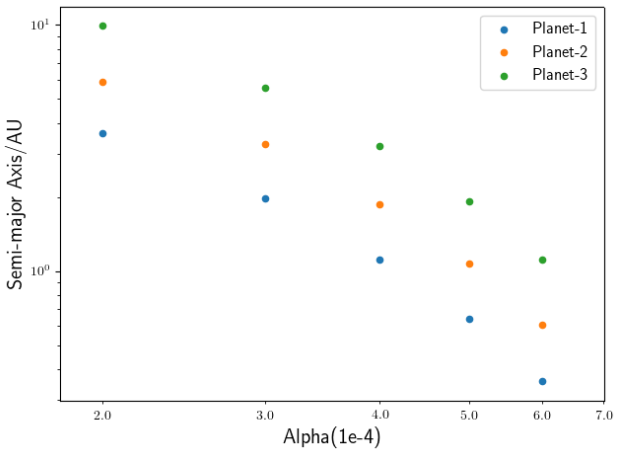

(a) Semi-major axis versus viscosity α.

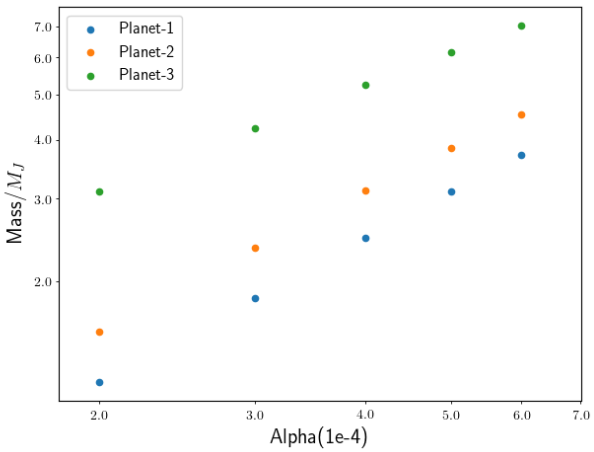

(b) Mass versus viscosity α.

Figure 6.7: Semi-major axis and Mass dependence on viscosity α.

and perform fitting to empirically see the trends. In each investigation, we plot a and m of each planet by varying only one free parameter and fix the other two free parameters to fiducial values. Figures 6.5, 6.6 and 6.7 show the break-down plots in different parameter spaces.

The dependence on flaring index f is shown by Figure 6.5a and 6.5b. As the flaring index increases from 0.15 to 0.35, the final semi-major axis decreases and the final mass increases. This can be explained by the global surface density profile solution equation (2.54), which implies $\Sigma \propto \nu^{-1}$. With a constant α, $\nu^{-1} \propto R^{-(0.5+2f)}$, therefore f controls the slope of the density profile. In the course of the inward migration, the surface density at the location of the planet increases more rapidly for larger f, which gives stronger positive feedback on both mass accretion and migration.

Figures 6.6a and 6.6b show that how the disk lifetime affects the final position and mass. As expected the final semi-major axis decreases and final mass increases when τ_{disk} increases from 1 Myr to 3 Myr. By definition $\tau_{\rm disk}$ is the e-fold lifetime of the disk, which determines the speed of disk dispersal. Planets in long-lived disk will simply have longer time to migrate and accrete and therefore larger and inner-migrated planets are expected for longer disk lifetime.

Finally, the dependence on the viscosity α is shown in Figure 6.7a and 6.7b. With an increasing viscosity, the planet tends to have stronger migration and accretion, as evident by the decreasing semi-major axis and increasing final mass. The key to understanding this dependence is the expression of K parameter equation (5.19). Since $K \propto \alpha^{-1}$, when α become larger, K becomes smaller; back to physical context, this means that a larger value of α favours faster diffusion as the diffusion timescale $\tau_\nu \propto \nu^{-1}$. Under this condition, the planet carve a shallower gap and as a result, planet will stay longer in Type I migration and have longer migration distance. The mass accretion dependence on K is similar if we recall equation (5.18). The accretion density Σ_{acc} is higher for a shallower gap, therefore planet gains larger accretion rate and grow larger.

6.2 Stable Evolution for the First 0.1 Gyr after the Disk-dispersal

After disk dispersal, we adopt the final states of the results at $3\tau_{disk}$ as initial conditions for the subsequent N-body simulation. We then evolve the systems for another 0.1 Gyr with gravitational force alone. At the time of this writing, 67 out of 75 cases were completed up to 0.1 Gyr. Due to the 240 hours limit of the CfCA computing system, the remaining 8 cases were not completed yet. In Figure 6.8, we plot an example of evolution of semi-major axis and eccentricity for three planets at 0.1 Gyr after the disk dispersal. In this case, there is no significant change of a and e within 0.1 Gyr, except tiny variations due to secular perturbations.

In fact, out of the 67 systems, no unstable case has been observed during the simulation, and the final states at 0.1 Gyr are almost identical to their initial states. Our result is largely different from the result of Simbulan et al. (2017), as they found most instabilities quickly occurs within million-year timescale, as shown by Figure 4.2. Therefore, in this section we will first compare our simulation with the previous empirical criteria of stability, and then we will discuss why our systems are more stable than the previous prediction.

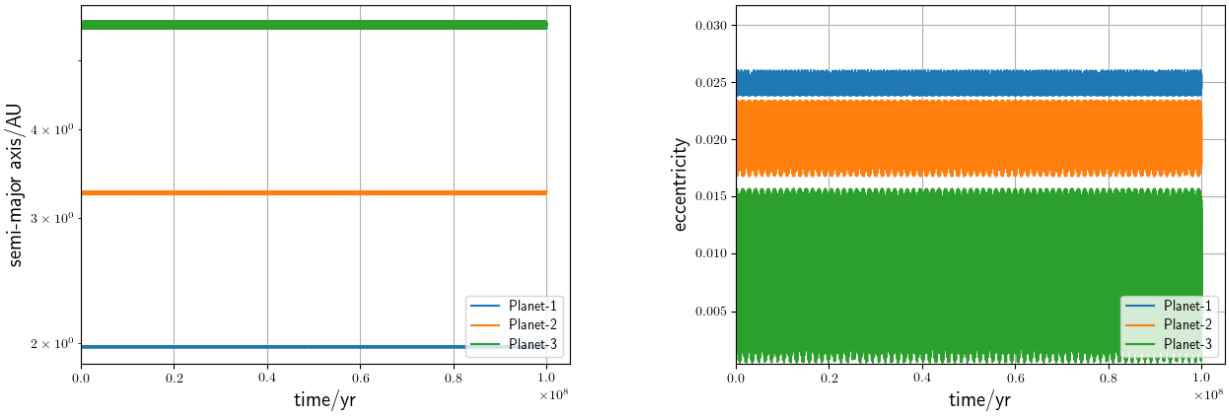

(a) Semi-major axis evolution

(b) Eccentricity evolution

Figure 6.8: Evolution of the semi-major axis and eccentricity for three planets ($f = 0.25$, $\tau_{disk} = 2\,\mathrm{Myr}$ and $\alpha = 3 \times 10^{-4}$).

6.2.1 Comparison with the Previous Criteria in terms of the Hill Radius

The past studies, e.g. Chambers et al. (1996); Marzari & Weidenschilling (2002), have shown that there exist a rough relationship between the instability time of a planetary system and the separations between adjacent planets in their mutual hill radius $R^H_{i,j}$:

$$R^H_{i,j} = \left(\frac{a_i + a_j}{2}\right)\left(\frac{M_i + M_j}{3M_*}\right)^{1/3}. \tag{6.1}$$

We further define a parameter K to be the separation of two adjacent planets divided by their mutual Hill radius:

$$K_i = \frac{a_{i+1} - a_i}{R^H_{i,i+1}}. \tag{6.2}$$

Particularly we define $K_0 = a_1/(M_1/3M_*)^{1/3}$. The "Hill Stable" criterion given by Gladman (1993) states that K has to be greater than $2\sqrt{3}$ in order to be stable. A recent paper, Wu et al. (2018), investigated on the stability criteria for 3, 4, 5 planet systems with a variety of mass distributions. The results suggested that the minimum of K values in a multi-planetary system, K_{min}, is the decisive factor that determines the dynamical instability time of a system, while the . By carrying out simulations in a wide range of parameter space, Wu et al. (2018) showed that the lower limit of the instability time t has a log-linear relation:

$$\log_{10}\left(\frac{t}{T_0}\right) = cK_{min} + d, \tag{6.3}$$

where T_0 is the orbital period of the innermost planet, c and d are constants. In the case of equally-spaced 3 planets with equal mass, Chambers et al. (1996) found that $c = 1.65$ and $d = 3.71$ for planet mass up to $10^{-5}\,\mathrm{M}_\odot$. Marzari & Weidenschilling (2002) investigated on the Jupiter-size planets($10^{-3}\,\mathrm{M}_\odot$) in the similar set-up and they obtained $c = 2.52$ and $d = -5.79$. The range of the K parameter that Chambers et al. (1996) investigated was around 2 to 10, whereas that investigated by Marzari & Weidenschilling (2002) was around 3 to 5.

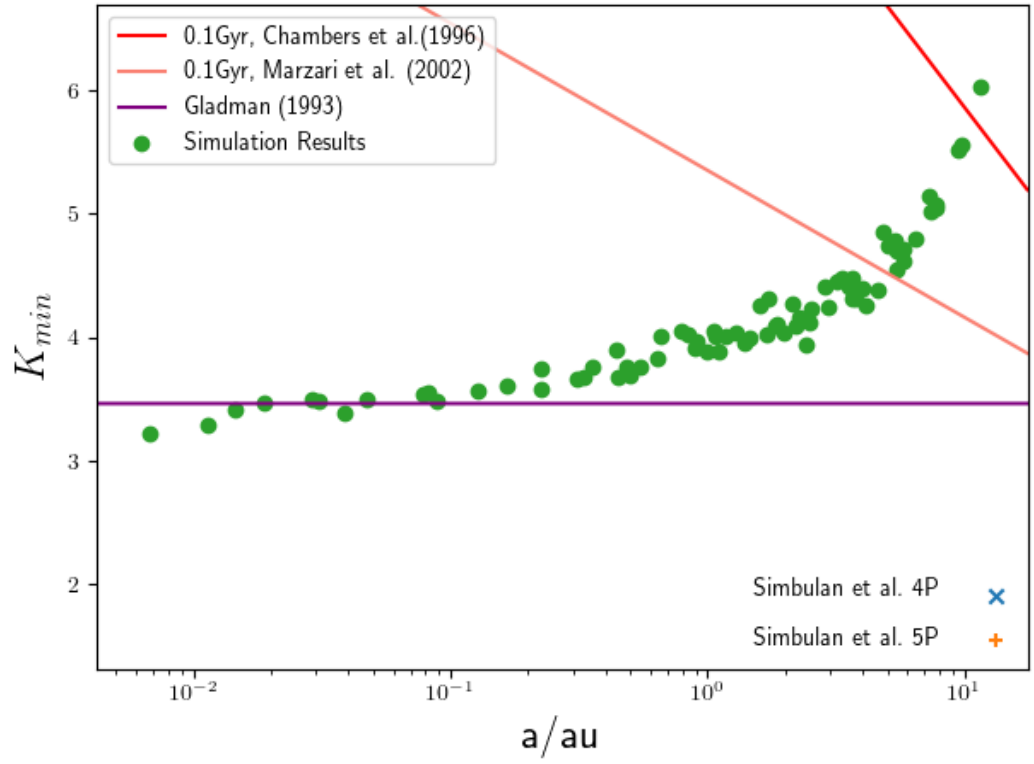

(a) K_{min} versus semi-major axis a/au.

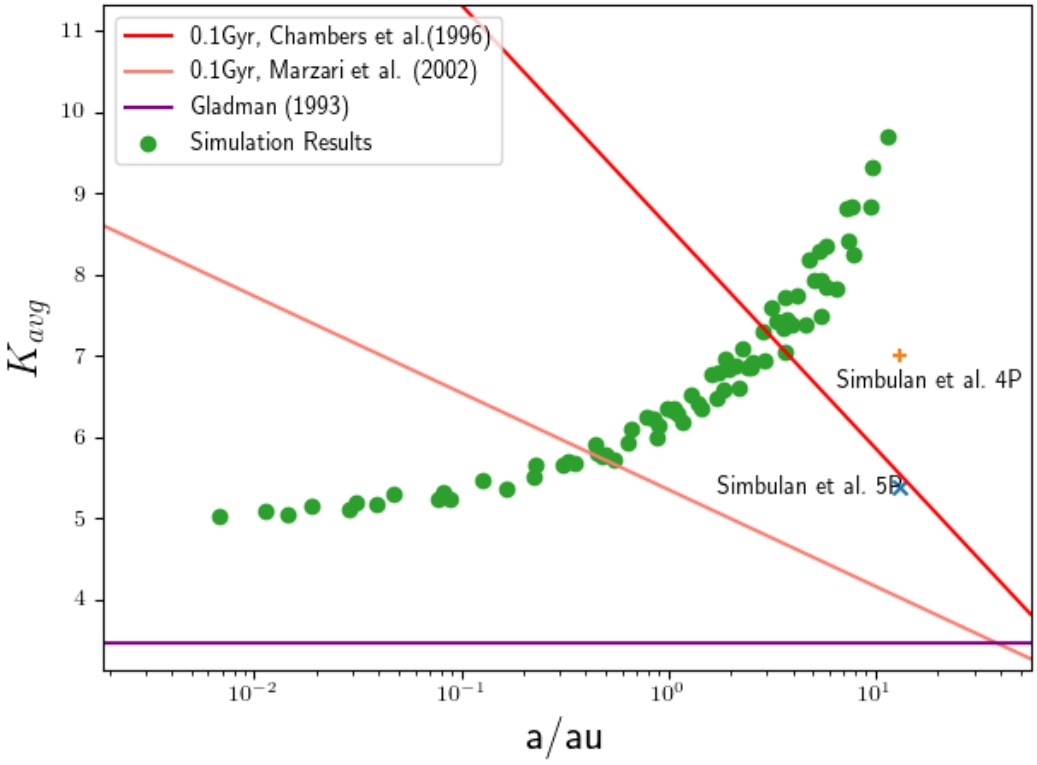

(b) K_{avg} versus semi-major axis a/au.

Figure 6.9: Plot of K_{min} against the semi-major axis/au of the innermost planet after $3\tau_{disk}$. Cross and plus signs are the results of the 4-planet nominal and 5-planet nominal cases of Simbulan et al. (2017). The red and salmon lines are the prediction of the 0.1 Gyr instability time based on the respective model, and the purple line is the Hill stable criterion given by Gladman (1993).

Figure 6.9 plots the K_{min} and K_{avg} of the all 75 systems at $3\tau_{disk}$. On the same plots we also add the 4-planet and 5-planet nominal cases of Simbulan et al. (2017) for comparison. We plot Gladman's Hill stability criterion and 0.1 Gyr lower-limit instability time line from both Chambers et al. (1996) and Marzari & Weidenschilling (2002). Figure 6.9a shows that most of the systems in our simulation are located above the Hill stable line, while Simbulan et al. (2017)'s systems are well below the line. In addition, almost all systems in our simulation stay at the left side of the 0.1 Gyr lower-limit instability time contours, which means the configurations of these systems are relatively stable as they survive much longer than the lower limit of the instability time. The plot of K_{avg} shown in Figure 6.9b reveals a similar pattern, and the conclusion on the instability comparison does not change qualitatively. From these results we may conclude that the planet-disk interaction has the stabilising effect on the configuration of the planetary systems, that is, systems which undergo migration and accretion are more stable than their counterparts with the same K_{min} but randomised initial conditions.

6.2.2 Hints to the Stability: the Period Ratios

The resonance between neighbouring planets can induce both instability and promote long-term stability of a planetary systemMalhotra (1998). To see whether planets have reached their resonance states, we plot the histogram of period ratios between adjacent planets, as shown by Figure 6.10. Figure 6.10a shows the period ratios just after $3\tau_{disk}$ and Figure 6.10b shows the period ratios at 0.1 Gyr after disk dispersal. We found both graphs show a clear cut-off at "2:1" resonance, which means most of the planet-pairs fail to enter major resonance states. This may be due to the fact that the migration coupling between two planets are too strong, so by the time the incoming planet reach resonance closer than 2:1, two planets already start co-moving. Larger than 2:1 period ratio, $P2 : P1$ shows different statistical distribution from $P3 : P2$. While $P3 : P2$ are widely distributed between 2.0 to 3.0 range, $P2 : P1$ are concentrating within the range from 2.0 to 2.4. This shows that the migration coupling between Planet 3 and 2 is stronger than that of Planet 2 and Planet 1.

To see how the period ratios vary with the parameter, we also plot the contour map of period ratio in the parameter space of the α viscosity and flaring index. The colour gradient stretching from bottom-left to top-right corner shows the clear trend that the period ratio monotonically increases with both flaring index and the viscosity. From the analysis in Section 6.1.3 we know that the migration speed also increases with these two parameters; therefore, it seems that the migration has the positive correlation with migration coupling. This agrees well with the above analysis that the migration coupling between Planet 3 and 2 is stronger, as the migration speed is higher for the outside planets at the early stage, shown by Figure 6.1d.

We may also compare the two histograms before the 0.1 Gyr evolution and after. While generally two histograms have similar distribution and range, one significant difference is that the histogram before 0.1 Gyr displays more small splitting than the other one. In Figure 6.10b there is also a larger spike at period ratio 2.05, where in Figure 6.10a the spike is not that pronounced. To account for these features, we may expect that planet systems are sufficiently interacted during the 0.1 Gyr evolution. To find the local minima of the gravitational potential, planets converge to nearby resonance or sub-resonance period ratios, leaving splits as well as enhancing spikes.

In addition, we plot the normalised histogram of period ratios of the all adjacent planet-pairs in

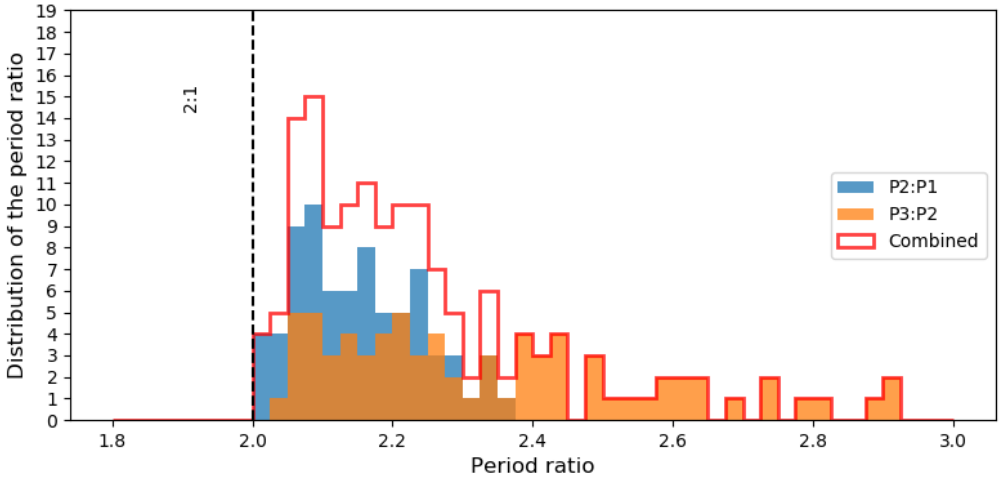

(a) Histogram of the period ratios after $3\tau_{disk}$.

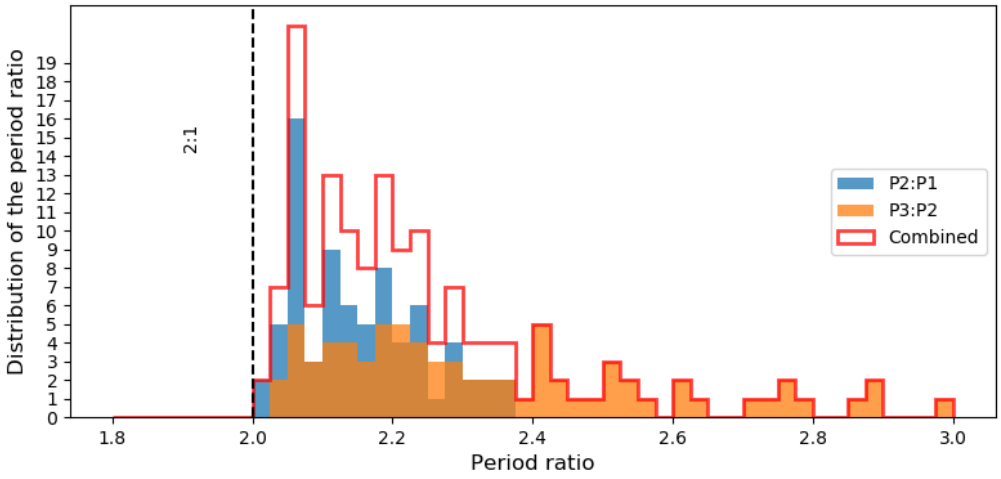

(b) Histogram of the period ratios at 0.1 Gyr after disk dispersal.

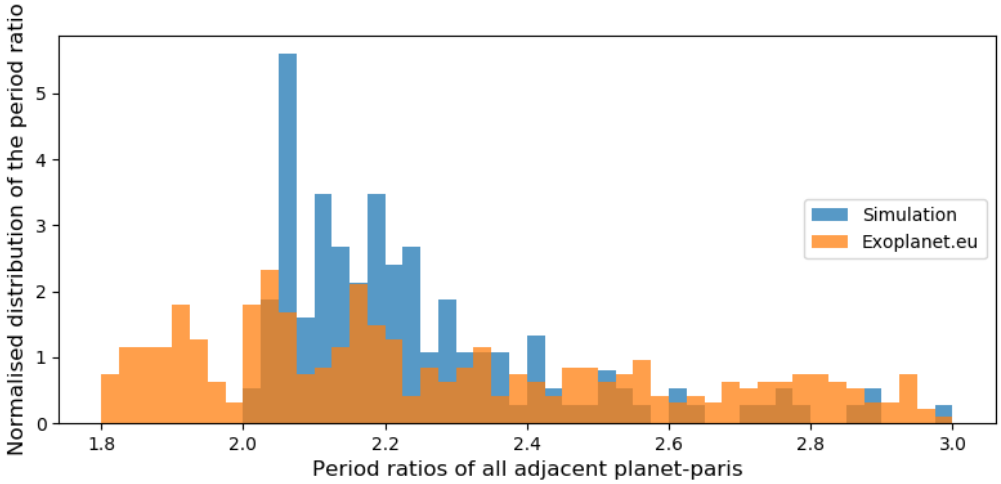

(c) Normalised histogram of the period ratios of the adjacent planet-pairs. Observational data is plotted from `Exoplanet.eu` database and simulation results at 0.1 Gyr after disk dispersal are compared.

Figure 6.10: Histograms of the period ratios. 'P2:P1' is the period ratio between Planet 2 and Planet 1. 'P3:P2' is the period ratio between Planet 3 and Planet 2.

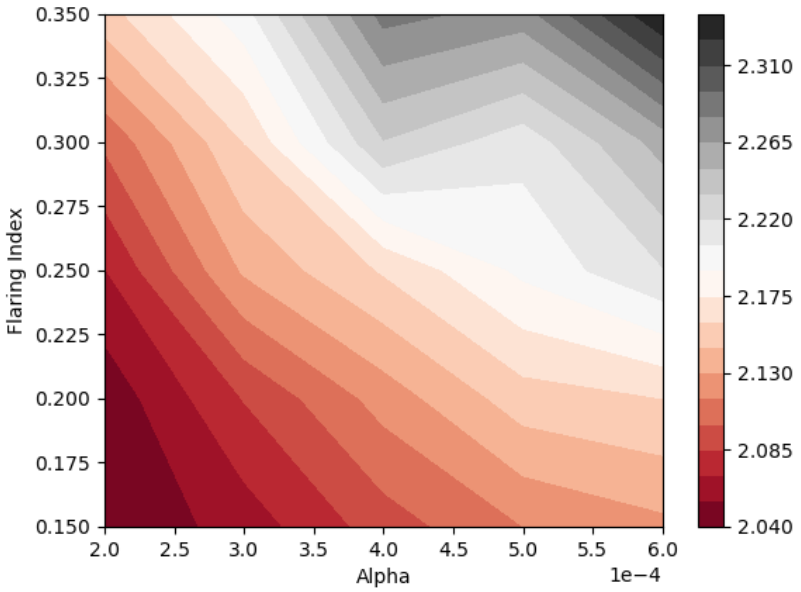

Figure 6.11: Contour Map of the Period Ratio P2:P1 after $3\tau_{disk}$. The two axis are α viscosity and flaring index.

Figure 6.10c using `Exoplanet.eu` database, and we find out that the simulation results do not agree with the observation data well. The observed period ratios clearly have a significant population smaller than 2.0, which is not reproduced by the simulation. Moreover, the observation data has a continuous tail extending from 2.6 to 3.0, while the our results show clear splitting at around 2.650, 2.825 and 2.950. The discrepancy between the simulation and the observation may suggest that the evolution of HL Tau system is not typical, i.e., there are other possible channels which contribute to the observed diversity of the planetary system configurations. It is also possible that some important physical mechanisms are missing in the current theories which can profoundly influence the evolution of planets before the disk dispersal.

we further investigate on this issue by plotting the evolution of both $P2 : P1$ and $P3 : P2$ period ratios up to $3\tau_{disk}$. The evolution of the $P2 : P1$ ratio lags slightly behind the $P3 : P2$ ratio because the outermost planet 3 starts to migrate first, then followed by planets 2 and 1. Since the migration time-scale is relatively small, the lag is negligible compared to the entire disk lifetime. Compared the fiducial case(Figure 6.12a) with other cases (Figure 6.12b, 6.12c and 6.12d), we find that regardless of the choice of free parameters, both periods quickly drop to around 2.0 in all four cases and then slowly increases until the disk almost disperses. This can be explained by our previous argument that the planets are bound to migrate together due to strong $2 : 1$ resonance. After reaching around the $2 : 1$ resonance, the migration coupling between the adjacent planets tends to 'repel' the planet and stop the planet-pair from being closer. Planet pairs in systems with smaller f, τ_{disk} and α only couple weakly, which means they can stay closer to the $2 : 1$ resonance. This agrees well with the trend of the final period ratios emerged from Figure 6.11.

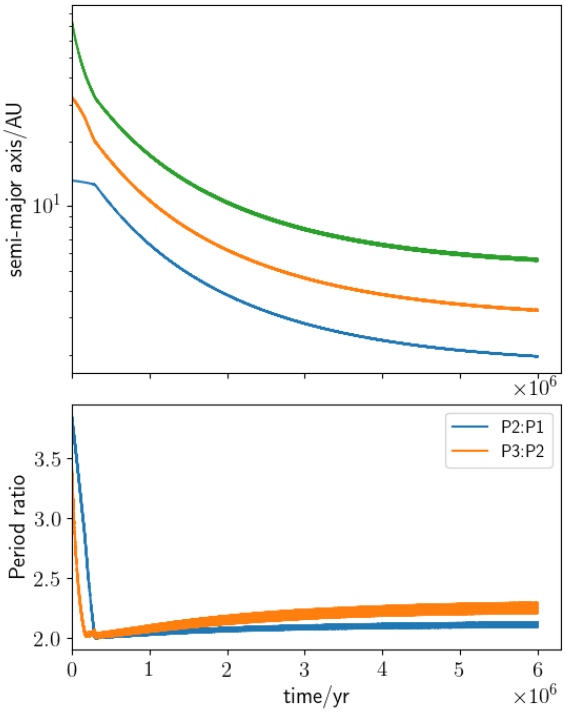

(a) $f = 0.25$, $\tau_{disk} = 2\,\mathrm{Myr}$ and $\alpha = 3 \times 10^{-4}$.

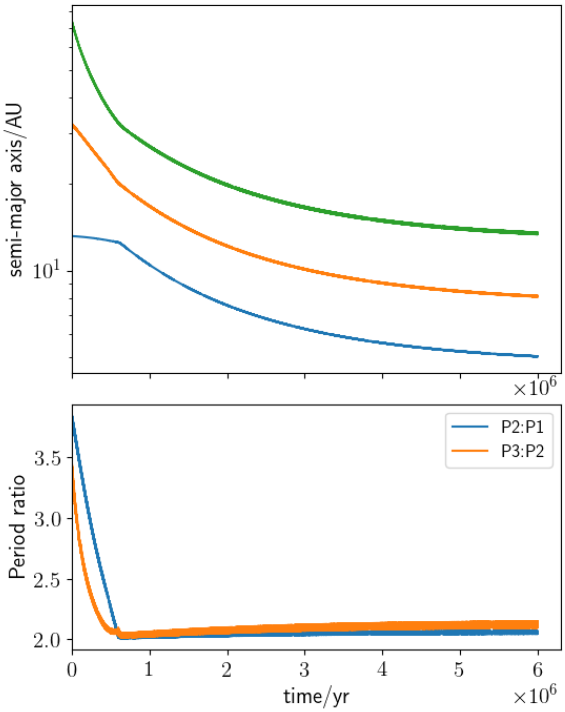

(b) $f = 0.15$, $\tau_{disk} = 2\,\mathrm{Myr}$ and $\alpha = 3 \times 10^{-4}$.

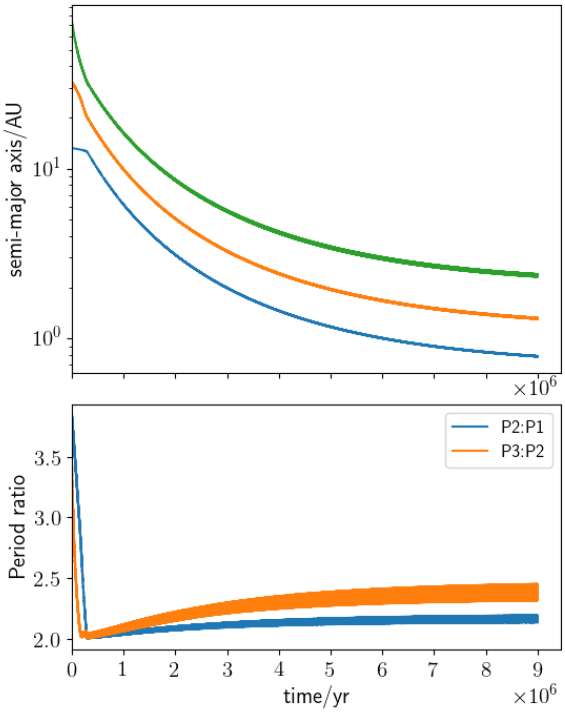

(c) $f = 0.25$, $\tau_{disk} = 3\,\mathrm{Myr}$ and $\alpha = 3 \times 10^{-4}$.

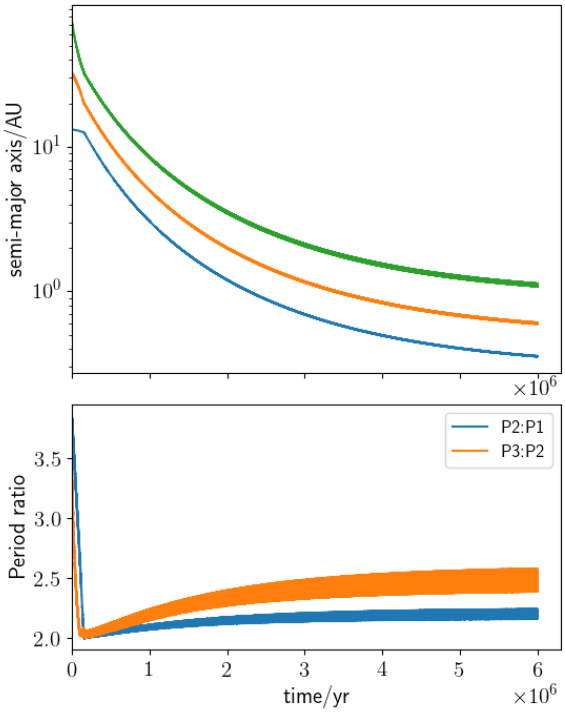

(d) $f = 0.25$, $\tau_{disk} = 2\,\mathrm{Myr}$ and $\alpha = 6 \times 10^{-4}$.

Figure 6.12: Evolution of the period ratios with different f, τ_{disk}, α.

Chapter 7

Conclusion

7.1 Summary

In this thesis, we review the structure and evolution of protoplanetary disk, the planet-disk interaction and planet-planet interaction, the observational facts as well as the pioneering work on HL Tau system. We build the theoretical framework that describe the evolution of planet inside a disk, including the equation of motion of a planet in a disk, modelling the surface density evolution in multi-planetary system and adoption of the migration/accretion model from the reference studies. For the numerical approaches, we implement all the interactions and incorporate them in the `REBOUND` simulation environment and we started simulations of the HL Tau system based on initial conditions derived from the current observations, each with three planets located at the deepest gaps. We also survey three free parameters, the flaring index f, the disk lifetime τ_{disk} and the viscosity α. In total 75 cases have been simulated and results are analysed in the respective parameter space. The simulation results after $3\tau_{\rm disk}$ show that the final semi-major axis of the planets ranges from around 0.007 au to 30 au, and the final mass of the planets ranges from $0.4\,\mathrm{M_J}$ to around $10\,\mathrm{M_J}$. After breaking down the results in different parameter spaces, we reveal and explain the trend that the final semi-major axis decreases while f, τ_{disk} and α increases, while the final mass of the planets increases as f, τ_{disk} and α increases. We further evolve the systems to 0.1 Gyr after the disk dispersal, and all systems remain stable and no significant changes occur. We explain the stability of the systems by investigating on the separation between planets in their mutual hill radius and we also statistically analyse the period ratios of adjacent planets. From the results we can conclude the the disk-planet interaction has stabilising effect on the planetary systems, as all the systems survive much longer than the lower limit of instability time predicted by previous studies and the majority of the planet pairs are not in the principal modes of resonance due to migration coupling. We investigate the period ratios between adjacent planet-pairs and find out none of the planet-pair is closer than 2 : 1 resonance. We further study the evolution of period ratios and find out that planet-pairs first approach 2 : 1 resonance due to the migration of the outer planet, and then move away from the 2 : 1 resonance due to migration coupling. This may imply that why the systems that we investigated are stable up to 0.1 Gyr since the migration coupling prevent the planet moving too close to instigate instability.

7.2 Future Work

There are a few ongoing work of this study. First, in our modelling of the disk, we assume that the disk is always in steady state rather than solving the disk diffusion equation in real time. We will consider adopting a more realistic disk model by including the real-time evolution of the disk structure. Second, the parameter space that we surveyed is also limited. We will examine a wider range of parameter space, such as adding inclinations, including more planets, and testing different mass distributions on the planet. We will continue evolving the system to Gyr time-sacle so as to check the stability criteria that we referenced. Third, we will expand our investigation to other HL Tau-like PPD system discovered by ALMA and see whether the results obtained from HL Tau is representative. We will compare our results with the current observation and eventually concluded on the possibility of reproducing the observed diversity of planetary systems from the initial configurations of planetary systems that we derived from the PPDs.

Appendix A

The Integrator tests

Before carrying out the actual simulation, it is important to know the accuracy that our numerical calculation can achieve; to ensure that the result is reliable, one has to know the performance of the integrator and tune the integrator by determining the optimal working parameters. We therefore perform two tests to examine the accuracy of the integrator: the conservation test and reproduction of the previous result. In the conservation test, we consider a two-body Keplerian system and evaluate the accuracy by checking the conservation of energy of the system. As a further check, we try to reproduce the N-body simulation results in Simbulan et al. (2017).

A.1 The Energy Conservation Test

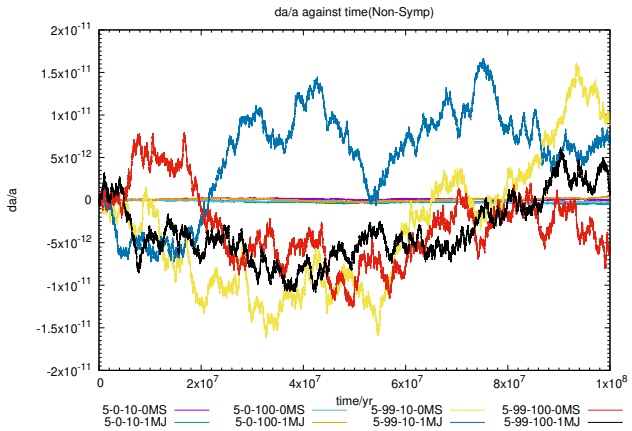

(a) Two body system which $a = 5\,\mathrm{au}$. The mass of the primary object is $1\,\mathrm{M}_\odot$. The formatted string key represents 'semi-major axis', 'eccentricity/100', '$\epsilon/10^{-11}$ ', and 'mass of the second body' respectively, where ϵ is the parameter that controls the error that the iterative loop intends to achieve. The same below.

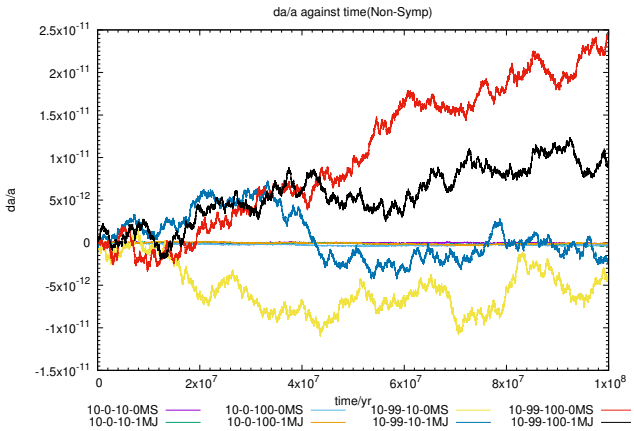

(b) Two body system which $a = 10\,\mathrm{au}$.

Figure A.1: Result of the energy conservation test.

The integrator `ias15` is a non-symplectic integrator with adaptive time-step. Although it is designed to achieve the machine precision (10^{-15}), the non-symplectic nature makes the energy conservation test necessary. We therefore consider a conservative two-body Keplerian system, perform the integration up to 10^8 yr and then evaluate the level of energy conservation in configurations with different orbital and integrator working parameters.

The results of the test are shown in Figure A.1. The color lines shows the time evolution of the fractional error of the semi-major axis a. For a two body Keplerian system, the energy E is a function of a only, therefore $dE/E \propto da/a$. The parameter space that has been surveyed includes a, the eccentricity e, the fractional error controlling parameter ϵ and the mass of the second body. For each of the parameter we tested two values, so in total there are 16 cases corresponding to 16 different lines in both Figure A.1a and A.1b. All fractional errors fall within the range of $O(10^{-11})$, and most of the cases the error is in the order of $O(10^{-12})$. The most significant factor that affects the error is the eccentricity, since the periastron distance at high eccentricity($e = 0.99$) is only 1 % of the circular case, resulting a larger error due to stronger interactions. At $e = 0$, regardless of other parameters, the fractional error is negligible and the good conservation near machine precision is achieved. The impact of ϵ parameter depends on the specific configurations: at low e the difference is negligible but at high e and a generally smaller ϵ performs better, as evidenced by Figure A.1b. The results also show that the conservation is rather insensitive to the the semi-major axis and mass.

Based on this result, we conclude that the `ias15` integrator generally can achieve a good level of energy conservation to the order of 10^{-12} within the parameter range that has been tested. Since planets are very closed to the circular motion inside the PPD due to eccentricity damping effect of the disk, choosing the default $\epsilon = 10^{-9}$ is sufficient to achieve a satisfactory level of conservation.

A.2 Reproduction of result in Simbulan et al. (2017)

Dynamical Events	Ejection	P-S Collision	P-P Collision	Remaining
Simbulan et al.	2.41	0.68	0.07	1.84
Our results	2.51	0.66	0.07	1.76
Fractional Difference(%)	4.15	2.94	0.0	4.35

Table A.1: Comparison between Simbulan et al.'s result and the reproduction test result. Number represents the averaged event rate per 5-planet system over 100 instances. "Ejection": planet ejected from the system with total energy > 0; "P-S Collision": collision events between planets and the central star; "P-P Collision": collision events between planets and planets.

We further check the reliability of the integrator by trying to reproduce the results stated in Simbulan et al. (2017). Using the identical initial condition, we initialised 100 instances of HL Tau system with 5 planets in non-resonant initial positions and integrated for up to 5 Gyr. All the dynamical events during the evolution, such as ejections and collisions, were also collected.

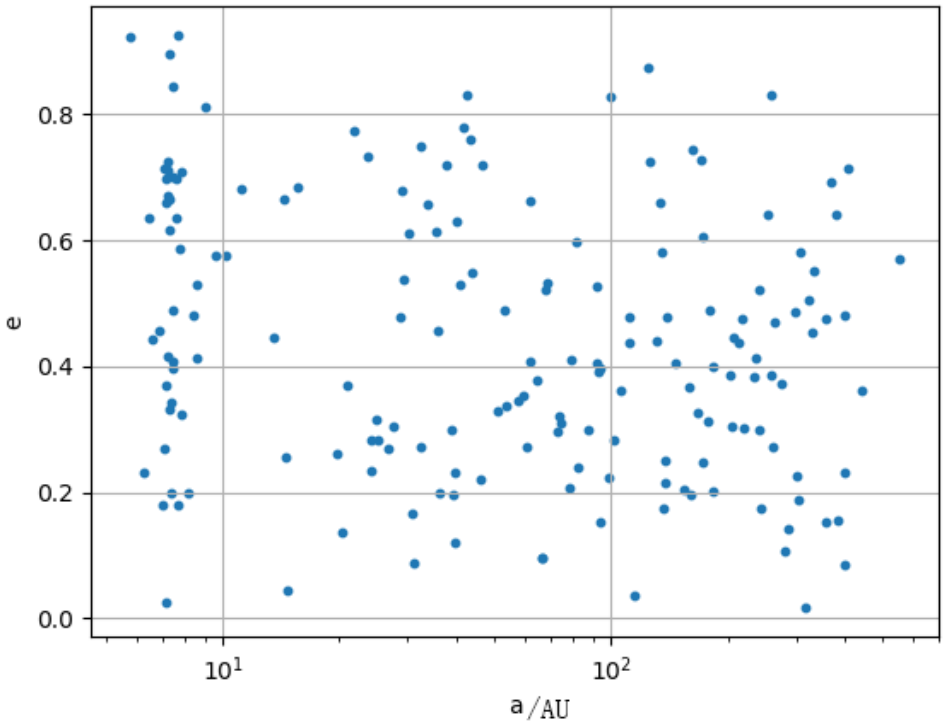

Figure A.2: Final distributions of the remaining planets in space of semi-major axis a/au and eccentricity e.

Figure A.2 shows the final distribution of eccentricity against semi-major axis of all the remaining planets, which agrees well with Simbulan et al.'s result: the "wall" of planet due to energy conservation at around $a = 7$ au is reproduced and the right boundary $a = 500$ au also coincides with the original figure. The statistical results of the dynamical events are summarised in Table A.1. For all types of dynamical events there is a good agreement with a fractional difference smaller than 5 percent, which can be attributed to the statistical fluctuation. We therefore conclude that the reproduction is faithful and the performance of the integrator meets our expectation.

Bibliography

Alexander, R., Pascucci, I., Andrews, S., Armitage, P., & Cieza, L. 2013,

Armitage, P. 2010, Astrophysics of Planet Formation (Cambridge University Press), 294

Armitage, P. J. 2015, arXiv e-prints, arXiv:1509.06382,

Batygin, K. 2012, Nature, 491, 418,

Chambers, J. E., Wetherill, G. W., & Boss, A. P. 1996, Icarus, 119, 261,

Chiang, E. I., & Goldreich, P. 1997, The Astrophysical Journal, 490, 368,

Crida, A., Morbidelli, A., & Masset, F. 2006, Icarus, 181, 587,

Duffell, P. C., & Chiang, E. 2015, The Astrophysical Journal, 812, 94,

Exoplanets.org. 2018, Exoplanets.org. `www.exoplanets.org`

Font, A. S., McCarthy, I. G., Johnstone, D., & Ballantyne, D. R. 2004, The Astrophysical Journal, 607, 890,

Gladman, B. 1993, Icarus, 106, 247,

Goldreich, P., & Tremaine, S. 1979, THE EXCITATION OF DENSITY WAVES AT THE LINDBLAD AND COROTATION RESONANCES BY AN EXTERNAL POTENTIAL 1, Tech. rep.

—. 1980, The Astrophysical Journal, 241, 425,

Hirose, S., & Turner, N. J. 2011, Astrophysical Journal Letters, 732, 30,

Kanagawa, K. D., Muto, T., Tanaka, H., et al. 2016, Publications of the Astronomical Society of Japan, 68, 1,

Kanagawa, K. D., Tanaka, H., Muto, T., Tanigawa, T., & Takeuchi, T. 2015, MNRAS, 448, 994,

Kanagawa, K. D., Tanaka, H., & Szuszkiewicz, E. 2018,

Kley, W., Peitz, J., & Bryden, G. 2004, A&A, 414, 735,

Kozai, Y. 1962, The Astronomical Journal, 67, 579,

Kwon, W., Looney, L. W., Mundy, L. G., & Welch, W. J. 2015, Astrophysical Journal, 808, 102,

Lee, M. H., & Peale, S. J. 2002, The Astrophysical Journal, 567, 596,

Lin, D. N., Bodenheimer, P., & Richardson, D. C. 1996, Nature, 380, 606,

Lin, D. N. C., & Papaloizou, J. 1979, Monthly Notices of the Royal Astronomical Society, 186, 799,

Malhotra, R. 1998, ORBITAL RESONANCES AND CHAOS IN THE SOLAR SYSTEM, Tech. rep.

Marzari, F., & Weidenschilling, S. J. 2002, Icarus, 156, 570,

Mayor, M., & Queloz, D. 1995, Nature, 378, 355,

Murray, C. D., & Dermott, S. F. 2000, Solar System Dynamics (Cambridge University Press). https://books.google.co.jp/books?id=-9FoswEACAAJ

Nagasawa, M., Ida, S., & Bessho, T. 2008, The Astrophysical Journal, 678, 498,

Paardekooper, S.-J., Baruteau, C., Crida, A., & Kley, W. 2010, Monthly Notices of the Royal Astronomical Society, 401, 1950,

Partnership, A., Brogan, C. L., Pérez, L. M., et al. 2015, The Astrophysical Journal Letters, 808, L3,

Pinte, C., Dent, W. R. F., Menard, F., et al. 2015, The Astrophysical Journal, 816, 25,

Pringle, J. E. 1981, Annual Review of Astronomy and Astrophysics, 19, 137,

Pringle, J. E. J. E., & King, A. R. 2007, Astrophysical flows (Cambridge University Press), 206. http://adsabs.harvard.edu/abs/2007af...book.....P

Rein, H., & Liu, S.-F. 2011, Astronomy & Astrophysics, Volume 537, id.A128, 10 pp., 537,

Rein, H., & Spiegel, D. S. 2014, Monthly Notices of the Royal Astronomical Society, Volume 446, Issue 2, p.1424-1437, 446, 1424,

Rybicki, G. B., & Lightman, A. P. 1979, New York, Wiley-Interscience, 1979. 393 p.

Sachs, A. 1974, Philosophical Transactions of the Royal Society A: Mathematical, Physical and Engineering Sciences, 276, 43,

Shakura, N. I., & Sunyaev, R. A. 1973, in X- and Gamma-Ray Astronomy (Dordrecht: Springer Netherlands), 155–164. http://www.springerlink.com/index/10.1007/978-94-010-2585-0{_}13

Simbulan, C., Tamayo, D., Petrovich, C., Rein, H., & Murray, N. 2017, Monthly Notices of the Royal Astronomical Society, 469, 3337,

Takahashi, S. Z., & Inutsuka, S.-i. 2016, The Astronomical Journal, 152, 184,

Takeuchi, T., & Lin, D. N. C. 2002, The Astrophysical Journal, 581, 1344,

Tanaka, H., Takeuchi, T., & Ward, W. R. 2002, The Astrophysical Journal, 565, 1257,

Tanigawa, T., & Tanaka, H. 2016, The Astrophysical Journal, 823, 48,

Toomre, A. 1964, The Astrophysical Journal, 139, 1217,

Walkowicz, L. M., & Basri, G. S. 2013, MNRAS, 436, 1883,

Wolszczan, A., & Frail, D. A. 1992, Nature, 355, 145,

Wu, D.-H., Zhang, R. C., Zhou, J.-L., & Steffen, J. H. 2018, Dynamical instability and its implications for planetary system architecture, Tech. rep.

Wu, Y., & Murray, N. 2003, The Astrophysical Journal, 589, 605,

Zhang, Y., & Jin, L. 2015, The Astrophysical Journal, 802, 58,